72. The Microstructure of Selective Palladium Hydrogenation Catalysts Supported on Calcium Carbonate and Modified by Lead (*Lindlar* Catalysts), Studied by Photoelectron Spectroscopy, Thermogravimetry, X-Ray Diffraction, and Electron Microscopy[1])

by **Robert Schlögl**[2])*, **Klaus Noack***, and **Heinz Zbinden**

Zentrale Forschungseinheiten, *F. Hoffmann-La Roche & Co. AG*, CH–4002 Basel

and **Armin Reller**

Anorganisch-chemisches Institut, Universität Zürich, Winterthurerstr. 190, CH–8057 Zürich

(16. II. 87)

A detailed analysis of the system Pd + Pb on $CaCO_3$ is presented. This system known as *Lindlar* catalyst is used for selective hydrogenations of C≡C bonds to C=C bonds. It was found to consist of seven distinct chemical phases. Essential ingredients are solid solutions of hydrogen and oxygen in Pd. The latter phase enables the metal particles to be attached to the support *via* an orientational relationship calcite (*113*)‖Pd + O (*111*). The addition of Pb neither changes the micromorphology of the disk-shaped Pd particles nor does it modify the electronic structure of Pd as studied by chemisorption experiments. The addition of Pb seems to block certain active sites and, thus, to enhance the selectivity. The support was found to be a multi-domain mixture of calcite and aragonite with domain sites of several hundred Å. The free surface of the pore-free solid is covered by a calcium-hydroxide carbonate. This phase as well as several other Pb phases seem to represent only spectator materials. Verification of this as well as finding the correlation between structure and function of the various components requires a kinetic analysis which is outside the scope of this paper. It is demonstrated that a variety of analytical techniques is required to unravel the complex nature of such a 'simple catalyst' as it is Pd on $CaCO_3$.

1. Introduction. – Pd supported on various materials is widely used as hydrogenation cataylst. A special variety, known as *Lindlar* catalyst, consists of Pd supported on $CaCO_3$, modified with Pb and further poisoned by organic bases such as quinoline. It is highly selective for the reduction of triple bonds to the (*Z*)-configurated double bonds [1] and has been the subject of various investigations. *Fukuda* and *Kusama* have studied the influence of the Pb concentration [2] and of the support material [3] on the hydrogenation of 1,4-butynediol and attribute to Pb a not further specified changing influence on the catalyst surface. One of the objectives of the newer investigations was to determine how the addition of Pb causes the high selectivity of typically over 95%. A recent publication [4] claims that the poisons (Pb and/or quinoline) have no specific effect on the reactive sites nor on the mechanism of the reaction, but merely cause the surface of the supported Pd to rearrange into larger crystals. *Palczewska et al.* [5] compare a specially prepared

[1]) The following abbreviations and acronyms are used in the text: b.e.: binding energy [eV], *BET: Brunauer-Emmett-Teller* (method of surface-area determination by physisorption of N_2), AES: *Auger* electron spectroscopy, XPES: X-ray photoelectron spectroscopy, UPES: ultraviolet photoelectron spectroscopy, ISS: ion-scattering spectroscopy, UHV: ultrahigh vacuum ($< 10^{-5}$ Pa), FTIR: *Fourier*-transform IR spectroscopy, TGA: thermal gravimetric analysis, XRD: X-ray diffraction, XDA: energy dispersive microanalysis, SEM: scanning electron microscopy, TEM: transmission electron microscopy, FWHM: Full width at half maximum.

[2]) Present address: *Fritz-Haber*-Institut, Faradayweg 4, D–1000 Berlin 33.

Pd-Pb alloy on $CaCO_3$ with a conventional *Lindlar* catalyst. They show that the alloy catalyst has a different H-sorption-desorption behaviour than the *Lindlar* catalyst. The latter chemisorbs H and forms the β-PdH phase, whereas the former only physisorbs H. The Pb in the *Lindlar* catalyst was found by XPES to be oxidized, and the alloy catalyst was claimed to contain Pb only in metallic form on its surface. The alloy catalyst was found to be more selective towards the formation of olefins. The authors [5] conclude that 'The uniform distribution of active sites, *i.e.* the fixed geometry of localization of Pb-atoms tailoring the two-dimensional oligoatomic cluster of Pd may explain the high selectivity'. Still other authors studied the effect of doping *Lindlar* catalysts with different metal salts and found that $MnCl_2$ can further enhance the selectivity [6]. The special role of the different hydrides of Pd in the hydrogenation reactions was reviewed by *Palczewska* [7]. The influence of the size of supported Pd particles on the hydrogenation [8] and on the hydride formation [9] was also studied: very small particles are less active as catalysts and do not form the β-PdH phase.

Lindlar catalysts are commercially available as powders of several micron mean particle size. They are air stable. The metal loading is typically 5 wt.-% with a very low dispersion of under 10%. The manufacturing process as it is described in *Lindlar*'s original publication [1] and in the procedure given in [10] involves only steps up to a maximum temperature of 85°. It starts with the fixation of Pd as hydroxide in aqueous solution followed by a reduction carried out also in aqueous solution. In a final step, Pb is precipitated from $Pb(AcO)_2$ onto the Pd-precursor catalysts.

It is empirically known that the nature of the support is of vital influence for the performance of the catalyst [3]. $CaCO_3$ exists at room temperature in the thermodynamically stable form of calcite and in two metastable forms of aragonite and vaterite. The exact precipitation conditions of the carbonate from aqueous solution determine the crystallographic modification which often can be a mixture of calcite and a metastable form. Prolonged contact of a metastable form of $CaCO_3$ with H_2O at room temperature causes its conversion to calcite. No obvious correlation between the crystallographic modification and the quality as *Lindlar* support could be established. Successful catalysts are prepared from pure calcite as well as from mixtures of calcite and aragonite.

The controversial views about the role of Pb in this catalyst prompted us to investigate the composition and structure of this multiphase system. We give a detailed description of our chosen sample catalysts in order to identify the essential ingredients which make up a *Lindlar* catalyst. We have employed a variety of techniques to study one experimental and several commercial catalysts. The techniques include powder XRD[1]), FTIR, thermal analysis, surface analytical techniques as XPES and UPES, ISS, AES as well as SEM and TEM. Without kinetic data, we do not attempt to elucidate the mechanism of the catalytic action. The catalytic activity of all catalysts used in this study has been tested under practical conditions. We will refer to these in a purely qualitative sense as 'good' or 'unsuccessful' in the description of our results. Concerning the controversial function of the Pb, we can definitely exclude several possible mechanisms but are unfortunately still unable to offer a definite conclusion.

2. Experimental. – 2.1. *Samples.* All samples and materials used in this study are summarised in *Table 1*. The two batches of the industrial catalyst *(Degussa CE 407 R/D)* came from different lots. Sample *746* was stored in air for two years before being used in this study. Sample *746* + was prepared only shortly before use. In catalytic tests on various substrates, there was little difference in activity and selectivity between the two batches.

Table 1. *List of Principal Materials Studied*

Designation	Description
746	Industrial catalyst; supplied by *Degussa AG* (5% *CE 407 R/D*), stored *ca.* 2 years before investigation; 5 wt.-% Pd, 4 wt.-% Pb, support *407*, a mixture of calcite and aragonite
746+	Same as *746*, second batch, prepared shortly before investigation
5% *E 407 R/D*	Industrial catalyst; supplied by *Degussa AG*; same support, same Pd loading as *746*, no addition of Pb, precursor for *746* and *746+*
407	Support of *746*, *746+*, and 5% *E 407 R/D*
408	$CaCO_3$ from *Degussa AG*, as comparison to *407*
603411	Experimental catalyst, made in *Roche* Laboratories, 4.7 wt.-% Pd precipitated on calcite
$Pd(OH)_2/CaCO_3$	As precipitated
$Pd(OH)_2/CaCO_3$	Heated subsequently *in vacuo* to 625 K = activated
$Pd(OH)_2/CaCO_3^{\ddagger}$	Heated subsequently in UHV to 790 K = heated
$Pd_{90}Pb_{10}$	Alloy of Pd and Pb as reference, prepared by rapid solidification in the splat-cooling process, *ca.* 30-mm disc, 100 mg
Pd	Reference, Pd foil, 0.5 mm, supplied by *Ventron*
Pb	Reference, Pb foil, 1.0 mm, supplied by *Ventron*
PdO	Reference, checked by powder XRD, supplied by *Roche*
$PbCO_3$	Reference, supplied by *Merck*

The experimental catalyst consists of precipitated $Pd(OH)_2$ (*ex* $PdCl_2$) on calcite. It was prepared similar to the procedure given by *Lindlar* [1]. One part was studied after the precipitation of Pd, one part was heated in a vacuum of 1×10^{-6} mbar to 350° for 24 h, and a third part was impregnated with Pb according to the original prescription after the thermal treatment. Catalytic testing showed the thermally treated sample to be highly active but very unselective. Impregnation with Pb improved the selectivity only slightly. A control sample of the non-heated Pd/calcite system was reduced by chemical means with HCOONa and impregnated with Pb. This catalyst was of good selectivity but considerably lower activity than the heat-treated samples. The overall performances of the experimental catalyst samples were not as good as those of the industrial ones.

2.2. *Apparatus.* Surface-area determinations were carried out with N_2 *BET* and Hg porosimetry using a *Carlo Erba* microstructure laboratory. Pore-size and particle-size determinations were carried out with the computer software supplied by the manufacturer. Thermal analyses were performed on a computerised *Perkin Elmer TGA 7* system. Heating rates were 10°/min, gaseous environments were N_2 and O_2. The XRD measurements were carried out on a *Siemens D 500* system equipped with a rotating sample holder. Cu-$K\alpha$ radiation with 1500-W power was used. A post monochromator and slits of 1° width before and 0.15° after the sample were used to improve background and resolution. Scans were made as step scans with 0.02° width and typically 20-s counting-time per step. FTIR were obtained on a *Nicolet FTIR 7199* spectrometer. Samples were prepared, in addition to KBr pellets, as nujol mulls to avoid any ambiguity in the detection of OH groups caused by the hygroscopic nature of KBr.

Surface analyses were performed in a *Leybold-Heraeus UHV LHS 11* surface-analysis system equipped with turbomolecular and Ti sublimation pumps allowing operation at a base pressure of 3×10^{-10} mbar. A special sample-introduction system attached to the preparation chamber allowed to investigate loose powders. Sample temp. between 80 K and 800 K (±1 K) were possible by means of a precision-regulated variable-temp. sample rod. A hemispherical analyser *LHS 11N* coupled to a microcomputer was used. XPES wide scans and X-ray excited AES were recorded at retardation ratio 8, for high-resolution XPES and ISS, the analyser was operated at constant pass energy of usually 50 eV. A twin anode Mg-Al X-ray source operated with 250-W power was used. Most of the spectra were recorded, however, with Mg radiation.

UPE Spectra were excited with a He discharge lamp (He(I) 21.2 eV, He(II) 40.8 eV). A scanning ion gun was used for both ISS (He) and sputter cleaning procedures (Ar). We note here that the catalysts are rapidly destroyed by Ar sputtering and have to be investigated without any surface treatment except prolonged outgassing in clean UHV. Accumulation times of 6 to 24 h were needed for the usually Mg-excited spectra displayed in this study. Binding energies were internally corrected for charging effects (see text) and related to Au $4f = 84.0$ eV. Numerical-data treatment included slight digital smoothing, linear background subtraction, integration, and, if necessary (for Ca 2p -Pd 3d spectra), satellite subtraction. Empirical cross sections were used for the quant. surface analyses [11]. Scanning electron microscopy was performed on Au-coated specimens in a *Jeol JSM 840* microscope operating at 15 or 25 keV. Backscattering detection was used to benefit from the contrast of Pd against the carrier. High-resolution TEM was performed on a *Jeol CX 200* microscope equipped with top entry stage and image intensifier. Specimens were dusted without the aid of any solvent onto Cu grids coated with a perforated carbon film.

3. Results. – 3.1. *Surface Areas.* The *BET* isotherms of sample *746* were of the same shape at all degassing temperatures of 100°, 200°, and 400°. The type-2 isotherm and the negligible hysteresis for the desorption branch characterise this catalyst as nonporous, *i.e.* as catalyst without micro- and mesopores. The *BET* standard areas were 11.0 m^2/g, 7.9 m^2/g, and 5.4 m^2/g for the three degassing temperatures. The surface of the pure support was determined at 200° to be 7.9 m^2/g. The second *746+* catalyst showed the same type-2 *BET* isotherm and exhibited a surface area of 7.1 m^2/g at 100° degassing temperature. The relative insensitivity of the surface area to various degassing temperatures is in line with a morphological study of the heat treatment of calcium carbonates which showed no visible change in morphology below 400°.

The surface area of the support (calcite) of the experimental catalyst was only 0.73 m^2/g. The precipitation of the Pd compound from aqueous $PdCl_2$ at pH *ca.* 1.0 increased the surface area to 3.3 m^2/g and to 4.2 m^2/g after thermal activation (all values at 100° degassing temperature). This is an increase of the surface of the pure calcite crystals by a factor of 5. This effect is not observed with the industrial catalysts. The specific pore volume increased from 0.007 cm^3/g for the support to 0.14 cm^3/g for the precipitated catalyst and decreased again down to 0.017 cm^3/g for the heat-treated catalyst. This is an indication for an etching effect of the acidic aqueous solution leaving the surface with a roughened morphology; subsequent thermal treatment burns off the reactive structures of the rough surface at temperatures below the bulk decomposition temperature of the support.

A particle-size distribution analysis from Hg porosimetry data showed for *746* a skew distribution with a maximum between 2 and 5 μm average particle size. The corresponding pore analysis showed the expected intergranular pores with a symmetric distribution around 1 μm. We interpret both results as an indication of a wide size distribution of uneven shaped particles.

The particle-size distribution and the intergranular-pore-size distribution for the experimental catalyst are extremely narrow. They show peaks at 5 to 10 μm particle size (74% of the relative volume) and at 6 μm for the intergranular pore size. The particles of this catalyst are of uniform size and shape.

Both results obtained from integral methods with several grams of sample are confirmed by observations in the SEM (see *Sect. 3.6.1*). The catalyst *746* consists of spherical aggregates of needles of below 10-μm size. A less common type of particles is rhombohedral in shape. The experimental catalyst consists of approximately cubic particles remarkably uniform in size and shape (*ca.* 5 μm).

3.2. *Powder XRD.* Powder XRD was performed on a series of samples including the pure support (*407*) of the catalyst *746*, the unused catalyst *746*, and the catalyst used once in a selective reduction reaction. The support proved to be a mixture of calcite and aragonite. The basic diffraction pattern of this mixture prevailed through all measurements. An example taken from a used catalyst is displayed in *Fig. 1*. The assignment of the two support phases is given by crosses for calcite and open circles for aragonite. In all diffractograms except that of the pure support, a third phase is present. It is indicated in *Fig. 1* with full circles and is assigned to $PbCO_3$ *(JCPDS 5-681)* [12].

The baseline of the diffractogram exhibits two broad structures around 39.5° and around 45° 2*θ*. These humps are the only indication of the Pd being present. No distinct *Bragg* reflection of either Pd metal or of a Pd-Pb alloy or of PdO or $Pd(OH)_2$ could be

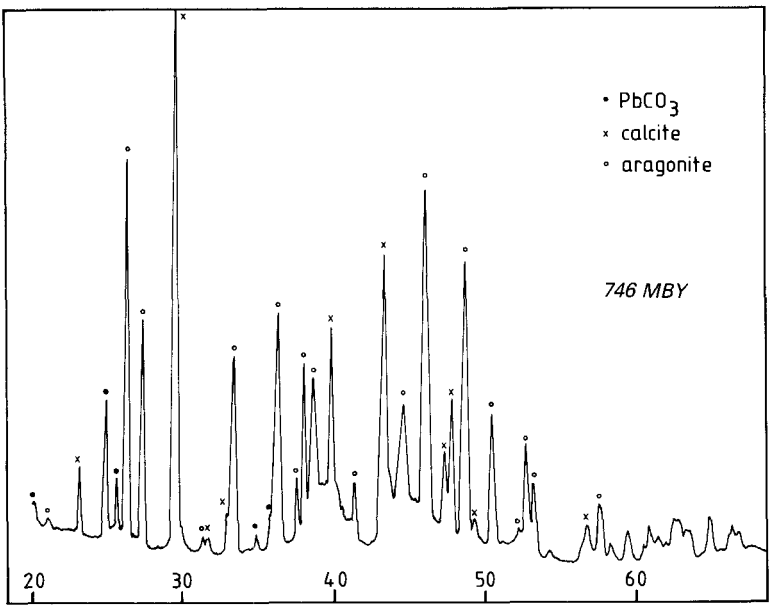

Fig. 1. *Powder XRD pattern* (Cu-K_α radiation, in air) *of the industrial catalyst* 746 *after catalytic testing*. The pattern is qualitatively the same for the unused catalyst. Note the deviations from a smoth background at around 40° and 45° 2θ which are the only indications for the presence of Pd.

identified. This result was confirmed by several film experiments with *Guinier* and *Gandolfi* cameras. Different irradiation times were used to verify that no extra lines were present except those found in the diffractometer traces.

During the search for possible Pd compounds, we performed a series of high-resolution XRD scans. A rotating sample holder was used to minimise orientation effects caused by the preparation of the specimen. In *Fig. 2*, which represents a small section of

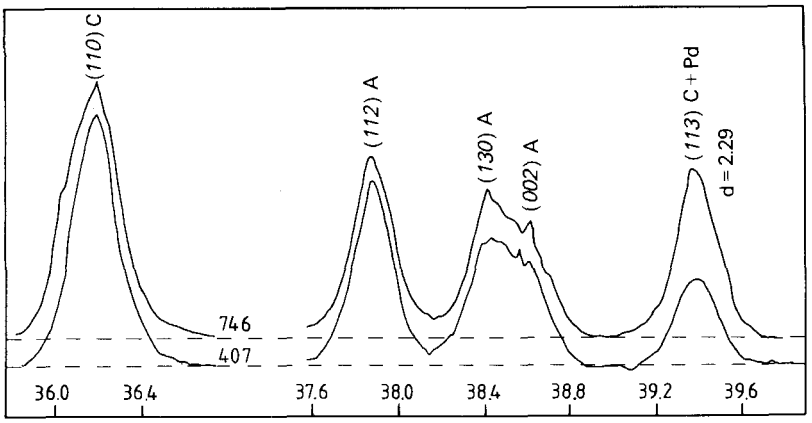

Fig. 2. High-resolution powder XRD scans of a small section seen also in Fig. 1. *746* is the unused catalyst, *407* its Pd-free support. The acquisition time was 12 h per scan. The (*110*) reflection of calcite, chosen for its proximity to the 2θ range of interest, nearly coincides with weak reflections of aragonite and $PbCO_3$. It was measured with much faster scan speed. Its intensity scale is reduced to match the main part of the figure.

the typical diffractogram from *Fig. 1*, we show that the intensities of the reflections of calcite and of aragonite in the pure support *407* and in the unused catalyst *746* agree quite well with each other except of those of the (*113*) reflection of calcite. This intensity deviation was found with the sample *746*+ as well. The experimental catalyst precipitated on pure calcite showed in this region a broad reflection centered exactly around the position for (*111*) of Pd at $d = 2.24$ *(JCPDS 5-681)* [12].

The extra intensity is ascribed to a Pd compound with crystallites of similar dimensions as those of the pure support (FWHM of the calcite (*113*) line with and without Pd is 0.24°, estimated natural line-width at that position is 0.12°). The d value of 2.29 is larger than that of (*111*) of pure Pd and slightly smaller than that of the (*111*) reflection of β-PdH with $d = 2.32$ *(JCPDS 18-951)* [12]. A rapidly quenched solid solution of 10 at.-% Pb in Pd showed its (*111*) reflection at $d = 2.26$. We attribute the extra intensity thus to a solid solution of oxygen in Pd. This will be further discussed in *Sect. 3.5*.

Inspection of the line-shapes of the diffractograms revealed that many of the aragonite peaks were broader than the majority of the calcite peaks (see also *Fig. 1*). Although we do not want to exactly interpret the line-broadening of the aragonite peaks in terms of a *Scherrer* analysis (particle shape, influence of stress during preparation of

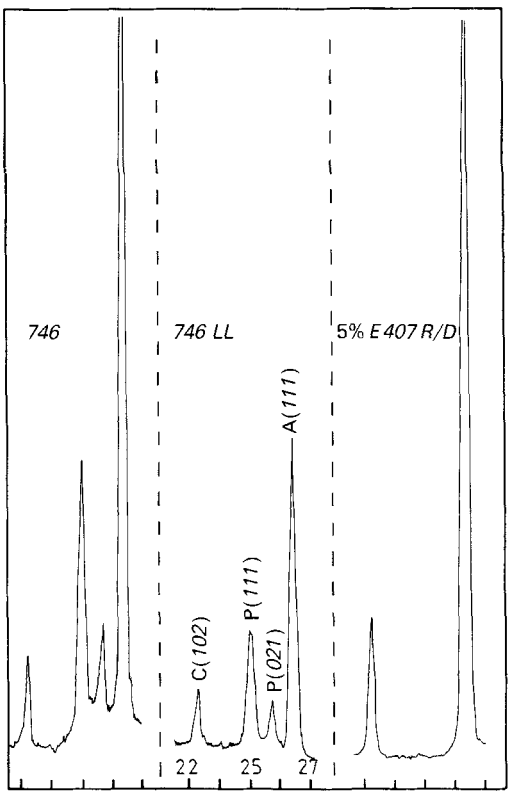

Fig. 3. *Part of the XRD traces of the Pd-impregnated support* (5% *E 407 R/D*), *of the unused final catalyst* (*746*) *and the used catalyst* (*746 LL*). Note the occurrence of reflections for $PbCO_3$ (*P*) after Pb impregnation and the changes in relative intensities of calcite (*C*) and aragonite (*A*) reflections after use.

the support *etc.*), we note that the average particle size is in the range of 10 nm. This means that the particles seen by Hg porosimetry as well as the morphologically uniform particles seen in the SEM (see *Sect. 3.6.1*) are polycrystalline. There was little systematic change of line-width with treatment of the catalysts.

The intensity ratios for the three phases calcite, aragonite, and $PbCO_3$ were found to vary with the use of the catalyst. The reflections in the range between 22° and 27° 2θ were chosen to monitor the changes. *Fig. 3* displays this region on an expanded scale. There is very little change in the intensities of calcite and aragonite between the pure support (not shown, *cf. Fig. 2*), the support after Pd fixation (right trace in *Fig. 3*) and the unused catalyst (left trace in *Fig. 3*). The addition of the Pb compound causes the reflections for $PbCO_3$ to appear (marked as 'P' in the central trace of *Fig. 3*). After one run in a catalysis experiment (central trace) both, the calcite-to-aragonite ratio and the ratio of $PbCO_3$ to calcite have changed. This is unexpected under the view that the reduction is carried out in a solvent- and nominally H_2O-free environment at room temperature. Taking into account, however, that the catalysts are used in concentrations of *ca.* 0.01 wt.-%, any impurities of the industrial organic substrates such as H_2O may well be in the same range of concentration and, thus, exert a modifying influence on the catalyst support. This was not a single observation but occurred with the sample *746* used in four different reactions.

The intensity ratios between calcite (*104*) at $d = 3.03$ (not shown in *Fig. 3*) and aragonite (*111*) at $d = 3.38$ were found to be 0.89 for the unused catalyst *746* and 1.70 for the sample after the reaction *'LL'*. The other used catalysts exhibited ratios between 1.24 and 1.76. The intensity ratio between calcite plus aragonite and $PbCO_3$ decreased systematically after use of the catalysts. It was 6.06 for the unused *746* and decreased to 4.47 for *746 'LL'* and was between 4.19 and 4.44 for the used catalysts in the other reactions. We state that these changes in crystallographic composition were associated with a certain activation of the catalysts during use.

3.3. *FTIR.* IR Spectra were used to obtain informations about the functional groups present on the surface of the unused catalyst. In *Fig. 4* spectra taken on nujol mulls are displayed for the catalyst *746*, for the pure support (*407*), and, as comparison, for an other support consisting of pure calcite (*408*). The spectra show the characteristic vibrations of $CaCO_3$ (annotated 1 to 4 and assigned to calcite (*c*) and aragonite (*a*), *'n'* denotes the C–H absorptions of nujol and *'h'* the broad absorption typical for H_2O and/or bridged OH groups). Three of the normal modes for the carbonate groups occur for both modifications with small shifts, one mode, ν_1, is in calcite only *Raman*-allowed and occurs, thus, only for the aragonite fraction in the spectra. The comparison of the spectra *407* and *408* allows to distinguish between the calcite and aragonite absorptions. Examining the relative intensities of the ν_2 absorption between the pure support and the final catalyst, one notes that the amount of aragonite seems to be larger in the final catalyst than in the support. Due to the quantitative inaccuracy of the nujol mull or KBr-disk spectra, no attempt was made to determine the exact ratios. No discussion of the line-shape of the intense ν_3 absorption is given for the same reason. We note that, with the XRD technique, this difference between catalyst and support was hardly detectable.

The pure supports and the final catalyst contain a significant amount of H_2O and OH groups on their surfaces, as can be seen by the intense OH absorption around 3400 cm^{-1}. The barely visible shoulder for the bending mode of H_2O at 1650 cm^{-1} identifies the OH

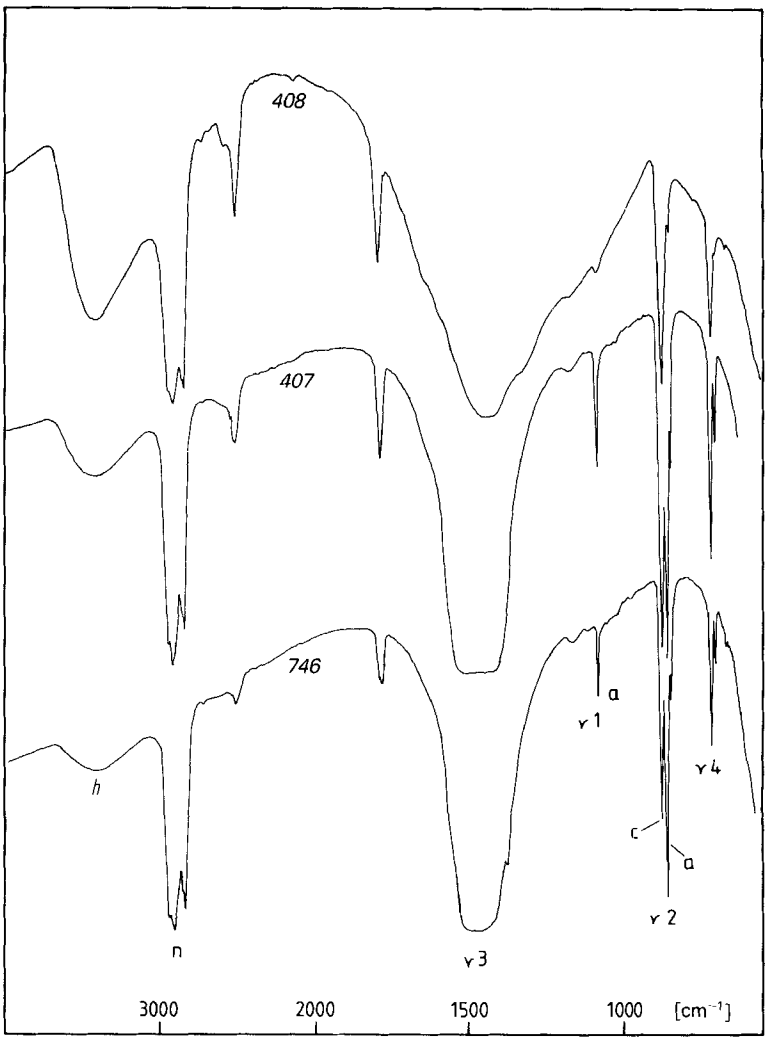

Fig. 4. *FTIR Spectra of nujol mulls* (n designates the nujol C–H absorptions). *408* is a pure support of (XRD) only calcite, *407* is the pure support of the *746* catalyst (calcite and aragonite), and *746* is the unused final catalyst. The two absorptions at *ca.* 2500 cm^{-1} and 1800 cm^{-1} occur in all spectra of carbonates, but their exact nature is unclear (see text).

vibration as to partly arise from molecular H_2O. This H_2O content is surprising, since $CaCO_3$ does not contain crystal H_2O, and a carbonate surface is not expected to bind large amounts of H_2O. Taking into account that many carbonates tend to react in moist air to hydroxycarbonates with solvation H_2O, we interpret these spectra as indication for the presence of such solvated hydroxycarbonates on the surfaces of the catalysts. The fact that we were unable to detect such phases in the XRD (*JCPDS 23-106* and *23-107*) [12] supports the view that these OH groups are located at the surface of the crystallites. It is advantageous that FTIR does not depend on particle size or crystalline order for the detection of such minority phases.

3.4. *Thermal Analysis.* Thermogravimetry was used as an integral method for characterization of both the surface and the bulk of the catalyst. The bulk characterization is performed by the observation of the decomposition of $CaCO_3$. It is known that the decomposition temperature depends on the modification of the carbonate [13]. In *Fig. 5* the decomposition curves are shown for the pure support (*407*), the Pd-loaded support (5% *E 407 R/D*), and for the final catalyst (*746*). The curves are shown for O_2 and N_2 gas environment, respectively. The curves for sample *746* were identical for the two gases (see also *Fig. 6*).

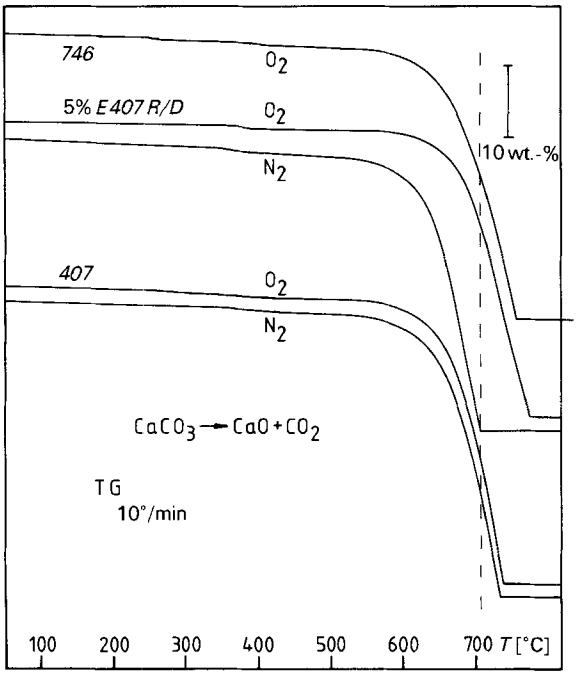

Fig. 5. *TG Survey scans showing the decomposition of the support. 407:* support, 5% *E 407 R/D:* support after fixation of the noble metal, *746:* final catalyst.

The decomposition temperature, defined by the temperature of 50% conversion, is 975 K for the support in N_2. We note that the reaction observed is in fact an equilibrium between oxide formation and uptake of CO_2 which renders the observed curves strongly dependent on the partial pressure of CO_2. This and the dependence of thermal data on particle size allow only to state general agreement with literature values ranging from 745 K to 1000 K [13]. The shape of the conversion curve is indicative of a single reaction. This implies that the material is homogeneous from the point of view of bulk chemical reactivity. Thus, the different crystallographic phases as seen by XRD and FTIR represent a thorough mixture with individual domains small enough to be averaged by the decomposition reaction.

The final catalyst and the pure support exhibit similar decomposition curves, whereas the one of the Pd-loaded sample without Pb is quite different. In particular, protective gas reduces the decomposition temperature significantly. Keeping in mind that the system

also contains traces of H_2O (see *Sect. 3.3*), we suggest that pure Pd helps the decomposition by catalytic conversion of CO_2 and H_2O to CH_4 which could reduce the partial pressure of CO_2 significantly. This reaction is known to occur with several transition-metal carbonate systems [14] and has been followed in this study in the UHV environment of the XPES spectrometer. In accordance with the TG observations, we found this reaction to proceed at *ca.* 350° easily for $Pd/CaCO_3$ and for $Pb/CaCO_3$, but not for the catalyst *746*. The difference in reactivity is an indication that, on a *Lindlar* catalyst, the support and the metals do not coexist as a physical mixture, but they form a unique phase with both metals and the support as ingredients. This phase seems to exhibit chemically different properties from those of the components. They are not confined to the observed catalytic selectivity, but are expressed also in the bulk chemical reactivity.

To follow surface decomposition reactions, the weight losses at high resolution are shown in *Fig. 6* for the same three systems as in *Fig. 5*. The pure support (*407*) exhibits two characteristic weight losses associated with the loss of molecular H_2O at 120° and with the decomposition of hydroxide at 450°. This was confirmed by thermal-desorption experiments in the UHV which showed the evolution of H_2O at both temperatures. From the fact that the characteristic temperatures were within 20° the same in the TG experiment at

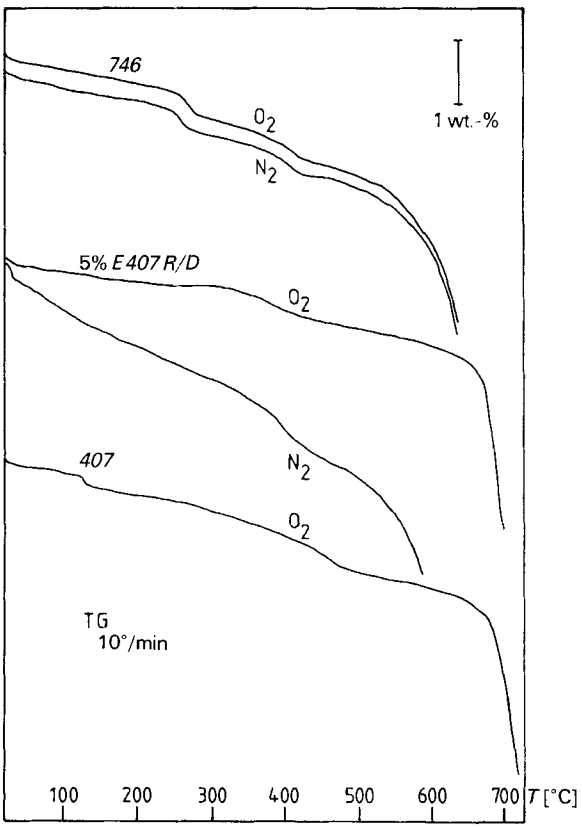

Fig. 6. *High-resolution TG scans of the low-temperature plateaus seen in* Fig. 5. The small steps at lower temperatures than the decomposition of the support indicate reactions of surface films.

atmospheric pressure and in the UHV environment at 1E-8 mbar, we deduce that the reactions occur largely at the surface where they are not hindered by diffusion.

The final catalyst (*746*) exhibits two similar weight losses, but they occur at different temperatures. The higher desorption temperature of 260° for molecular H_2O indicates that the majority of sites which hold H_2O are modified by the preparation of the catalyst. Most of them are not blocked by Pd due to its low dispersion (see below).

Pure Pd on the support (5% *E 407 R/D*) is different again. The hydroxide decomposition is observed at 410°, similar to the final catalyst, whereas there is almost no desorption of molecular H_2O in a characteristic step. It is desorbed in continuous way starting with the desorption of physisorbed H_2O (see left edge in the central two curves) up to the hydroxide decomposition at 410°. The difference of the decomposition in O_2 and in N_2 atmospheres between 100° and 500° is attributed to a reaction of the Pd with O_2 leading to an increase in weight which nearly compensates for the loss due to the desorption of H_2O. We note that this reaction which could lead to PdO and/or a solid solution of oxygen in Pd does not occur in the Pb-modified catalyst. This is in agreement with the observation from XRD (see *Fig. 2*) that in the catalyst *746* the Pd is present already as a solid solution with oxygen.

During the thermal desorption experiments, we observed that the evolution pattern of H_2 allows a distinction between Pd present as $Pd(OH)_2$ or present as PdO. In *Fig. 7*, the corresponding curves are displayed. Both catalysts *746* and *746+* showed similar desorption patterns. All Pd compounds and Pd foil released H_2 above *ca.* 400°. Only $Pd(OH)_2$ (supported on calcite) showed a second desorption at lower temperature. This desorption is followed by a change in the formal oxidation state of Pd detected by XPES (see *Sect. 3.5.4*). The decomposition of $Pd(OH)_2$ into Pd metal, H_2, and O_2 causes the H_2

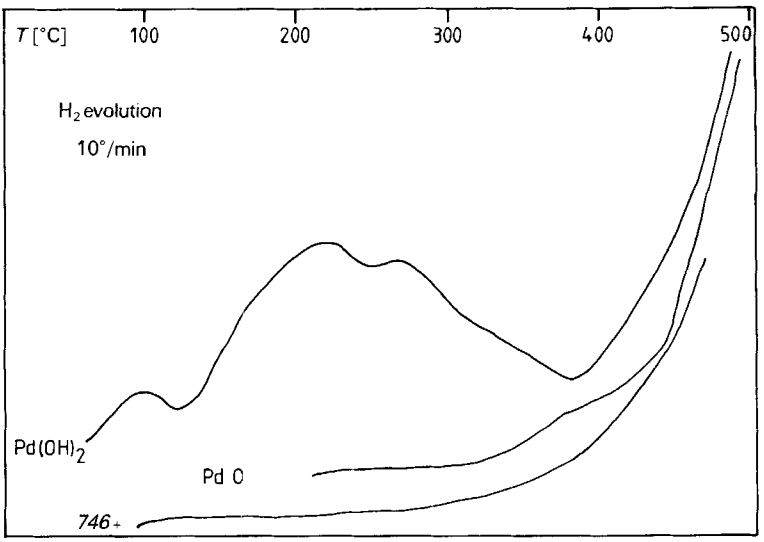

Fig. 7. *Thermal desorption of H_2 from Pd samples.* $CaCO_3/Pd(OH)_2$ is the experimental catalyst before any heat treatment, PdO is a reference sample, and *746+* is the new batch of the industrial catalyst. The other batch of *746* exhibits the same behaviour. The measurements were carried out in the UHV chamber of the photo-emission apparatus. The quadrupole mass spectrometer output for m/z 2 was used to construct this figure.

evolution. An analogous behaviour is known for Ni [15]. Pd foil, loaded with hydrogen at 50° under atmospheric pressure (formation of α-PdH), gives off most of its hydrogen in a similar curve to the hydroxide. The catalysts *746* and *746+* contain, thus, the Pd neither as $Pd(OH)_2$ nor as α-PdH. The hydrogen evolution at high temperature is common to all kinds of Pd subjected for the first time to thermal desorption and is, thus, of little diagnostic value.

3.5. *Electron Spectroscopy.* In the following, we present the results of the surface investigation with electron spectroscopy. We have selected typical sample spectra for each core level to minimise the number of displayed items. To see the connection between the spectra, we briefly describe the strategy of data acquisition. All reference values for b.e.'s[1]) were obtained from measurements of standard samples under the same experimental conditions as the spectra of the catalysts. After outgassing, all core level spectra were recorded for a short time and subsequently for *ca.* 12 h. Comparison allowed to estimate sample deterioration during data acquisition. In general, the stability was excellent after sufficient outgassing (typically overnight at room temperature). After the data collection for the *Auger* lines, the samples were heated *in situ* to temperatures where, in pilot experiments, characteristic points in the desorption patterns had been identified with a quadrupole mass spectrometer. Temperatures above 800 K were not possible due to the massive CO_2 evolution from the decomposition of the support.

In *Table 2*, a collection of b.e.'s is presented. All values are corrected for charging (see *Sect. 3.5.2*) and relate to a calibration against Au $4f_{7/2}$ at 84.0 eV. The values for C and Ca are consistent which each other: in all samples the support gives a similar spectrum. In some cases, the Ca 2p spectrum exhibited a shoulder at higher energy which is due to

Table 2. *Binding Energies for Various Catalysts and Reference Compounds.* All values in eV[a]).

Sample	C 1s	O 1s	Ca $2p_{3/2}$	Pd $3d_{5/2}$	Pb $4f_{7/2}$
746	289.7	531.3	350.7	336.2	138.5
			347.3	334.6	136.4
746+	289.9	532.0	347.7	336.4	138.6
				335.0	137.1
746+ (790 K)	289.7	531.7	347.3	336.2	136.9
				334.8	136.0
5% *E 407 R/D*	289.5	531.3	350.6	336.0	–
			347.1	334.9	
603411[b])	284.7	530.8	n.o.	337.3	–
$PbCO_3/CaCO_3$	289.7	531.4	350.0	–	137.6
			347.8		
$PbCO_3$	289.9	531.0	–	–	138.7
PdO (300 K)	–	530.6	–	337.5	–
PdO (560 K)	–	530.5	–	336.3	–
				335.0	
Pd foil, sputter-cleaned	–	–	–	335.1	–
Pb foil, scratched	288.4	530.8	–	–	137.5
	284.7	529.0			136.1
Pb foil, sputter-cleaned	–	–	–	–	136.1
$Pd_{90}Pb_{10}$, sputter-cleaned	284.6	532.5	–	335.4	136.9

[a]) Error in determination of the peak positions ±0.1 eV. Reproducibility ±0.2 eV.

[b]) In sample *603411*, the support is not detectable: the C 1s value is the C contamination without any charge correction, the Ca 2p spectrum is not visible.

CaO. A slurry of precipitated $Ca(OH)_2$ was heated to 600° inside the spectrometer. After this treatment, a Ca 2p peak at 350.7 eV was obtained.

3.5.1. *Wide-Scan Spectra.* These spectra acquired with medium resolution are used to detect impurities in the samples studied. After typically 12-h measuring time, spectra as displayed in *Fig. 8* for the catalyst *746* were obtained. We recognize most of the core levels

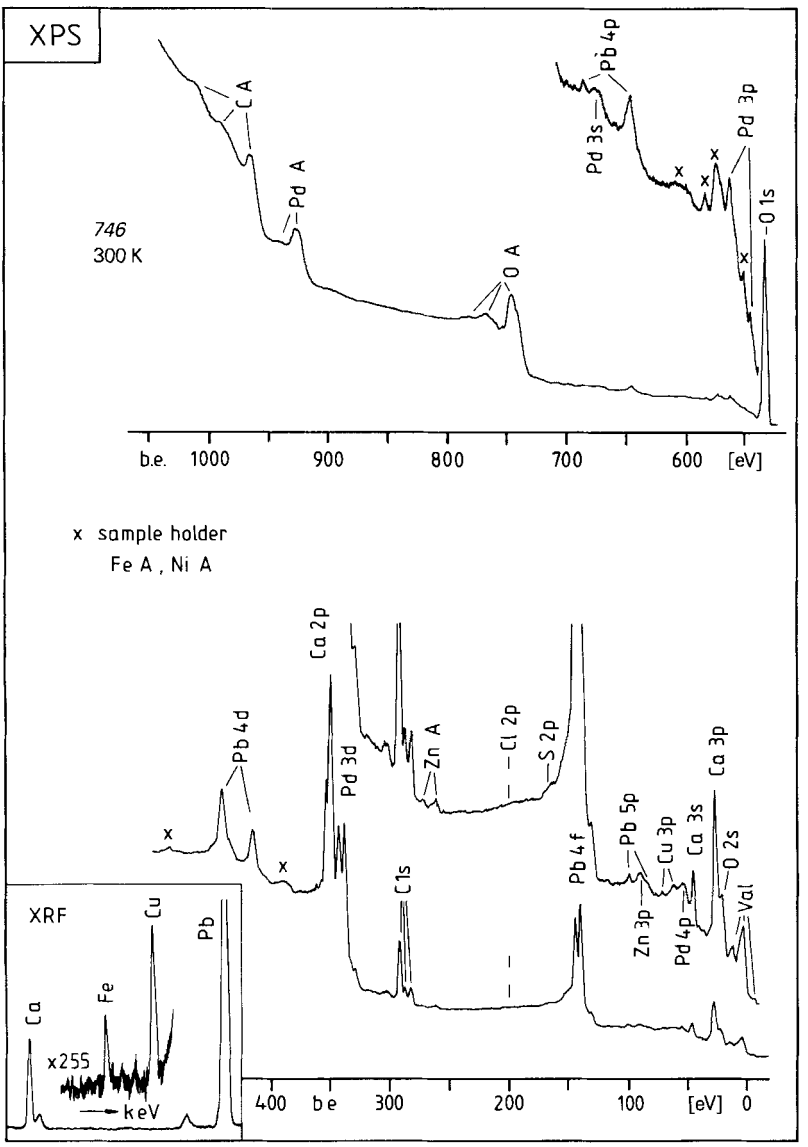

Fig. 8. *XPES Survey spectrum of the industrial catalyst.* Only small amounts of impurities were detected. The inset shows an X-ray fluorescence spectrum taken from the powder catalyst with Mo radiation. The crosses in the XPES data designate peaks arising from the materials of the sample holder (Fe and Ni). XRD shows that Fe is also an impurity of the catalyst.

and the much wider structures arising from the principal *Auger* transitions for the four elements present in the catalyst. There is no indication for the expected impurity of Cl, whereas we detect traces of S as sulfate. Cationic impurities were Zn and Cu. Traces of Fe which were detected by X-ray fluorescence analysis (XRF; see inset in *Fig. 8*, Mo excitation) may be hidden under the spectrum of the edges of the sample holder (stainless steel) which becomes visible after long accumulation times. Both industrial catalysts proved to be very pure in the sense of these XPES wide scans, the experimental catalyst contained a significant amount of Cl as impurity. To illustrate the problems associated with analysis of the Pd species, note the small peak at zero energy in *Fig. 8* (designated 'Val', far right feature) which arises from the Pd 4d valence band. This peak contains valuable information in its shape and was measured in high resolution (and thus low intensity) for all samples. This peak is discussed in detail with *Fig. 14 (Sect. 3.5.4)*.

3.5.2. *Carbon Spectra.* All our catalysts are electrical insulators. In the photo-ionisation process, the industrial catalysts were electrically charged; this causes shifts of the energy scale of several eV. Fortunately, the C 1s spectra provide an internal standard for correcting these charging phenomena. In *Fig. 9*, the high-resolution C 1s spectra for samples *746* and *746+* are displayed. We expect for carbonate a single peak located at about 5 eV higher b.e. than for elemental C. We observe, however, three peaks. The assignment of the peak at highest b.e. to carbonate C is unambiguous from charge-density arguments. The two other peaks vary in relative intensity, separation, and shape from sample to sample. The separation between the central peak and the carbonate is with 5.0 eV constant for all samples. Both of the varying peaks represent hydrocarbon contamination of the surface. An additional source for C is the X-ray-induced decomposition of $CaCO_3$ which was found to occur with samples of small particle size. The differences

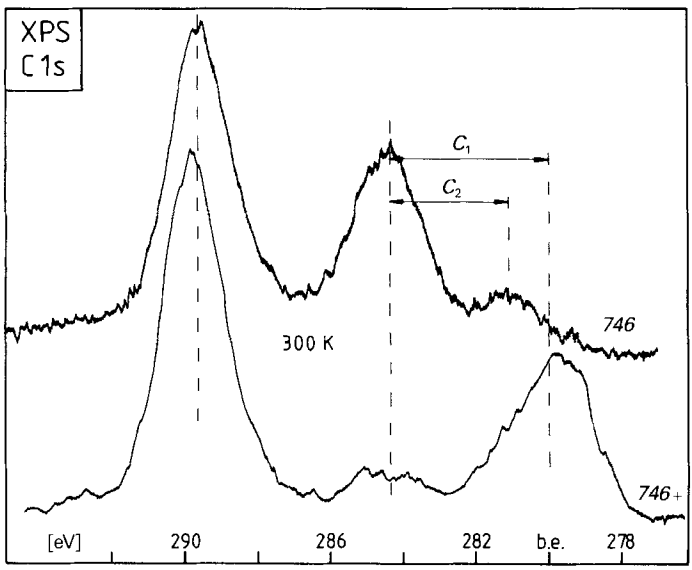

Fig. 9. *C 1s High-resolution spectra of the two industrial catalysts.* The energy differences C_1 and C_2 indicate the charging corrections which have to be applied to construct a common energy scale for all samples (see text). The peak at *ca.* 289 eV arises from the carbonate anions in both samples.

between the two peaks (marked in *Fig. 9* as C_1 and C_2) arise from the electrostatic field between parts of the sample surface and the grounded spectrometer, *i.e.* from charging. Our instrument allows to modify this electrostatic field by applying a variable voltage to a tubular electrode in the analyser assembly. By applying different voltages, we thus were able to influence the separations C_1 and C_2, but not the distance between the central line and the carbonate peak. This justifies the procedure of charge correction which consists of shifting of the energy scale by the value of the correction constant C (C_1 for *746+*, C_2 for *746*). This has been done for all *Figures* (including *Fig. 9*) and binding energies quoted hereafter. The difference between C_1 and C_2 illustrates the necessity for this charge correction. Even among the data of the various catalysts, there would be little consistency of the data without this correction.

After correction for charging, we obtain a value of *ca.* 289.7 eV for carbonate C. The contamination peak at 284.7 eV is typical for aliphatic C. Both lines are wider than expected. The line-broadening is, at least in part, due to the electrostatic inhomogeneous sample surface (differential charging, as seen by the two contamination peaks). We note that the contamination peaks are somewhat asymmetric. This could point to molecular structure of H–C–O groups as part of the contamination. In the FTIR spectra, we found two absorptions at *ca.* 2500 cm^{-1} and at *ca.* 1750 cm^{-1}. In the thermal desorption experiments, we observed at *ca.* 300° the desorption of a species with mass 30 (CH_2O).

3.5.3. *Oxygen Spectra.* Oxygen is the most abundant element on the catalyst surfaces (see *Sect. 3.5.6*). Sources are the various carbonates, H_2O, OH groups, and possibly oxygen in Pd. The spectra observed were typically of the shape displayed in *Fig. 10*. They

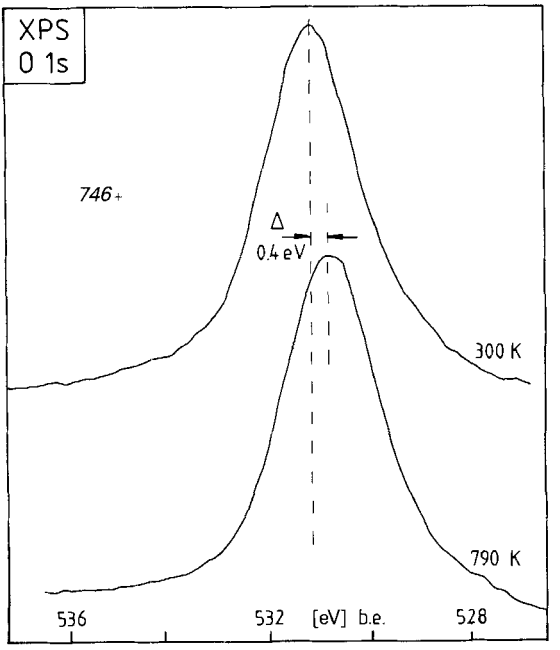

Fig. 10. *O 1s High-resolution spectra of the new batch of the industrial catalyst at two temperatures.* Note the small shift and compare to the shift of Pd 3d shown in *Fig. 12*.

show little resolution. The presence of several species is indicated, however, by the line-shapes (intensity in the wings of the peaks) as well as by the line-widths between 2.2 eV and 2.4 eV (top and bottom trace, respectively, in *Fig. 10*). Single-species oxides exhibit typical widths of 1.5 eV. The b.e. of 531.2 eV at room temperature is indicative of a hydroxide surface. The dry oxides of Ca, Pb, and Pd show b.e.'s of below 530.6 eV. Heating the sample to 790 K for 12 h resulted in a slight shift to lower b.e. This hydroxide is not an adsorbed species but represents a layer of a thickness much above the information depth of XPES. This layer is not uniformly distributed over the whole sample surface, but covers only part of the carbonate. This non-uniformity of the surface of the catalysts makes any quantitative evaluation rather uncertain (see also *Sect. 3.5.6*). Comparison with the TG results *(Fig. 6)* shows that a thin hydroxide layer would have been decomposed at that temperature. The hydroxide is so stable under 790 K UHV conditions that the surface probed by XPES is only converted to CaO, if all the rest of the underlying bulk has reacted. The MS recorded during data acquisition for XPES showed the presence of small amounts of H_2O indicating that the diffusion hindered process of hydroxide decomposition is still going on.

The oxygen KVV *Auger* spectra allowed a better distinction of the various O species. In *Fig. 11*, the complex spectrum of the catalyst *746* is compared to that of the experimental catalyst (*603411*) and that of PdO. The labelling serves as crude reference for the shift range in the *Auger* transition. The label 'CaO' stands also for calcium hydroxide.

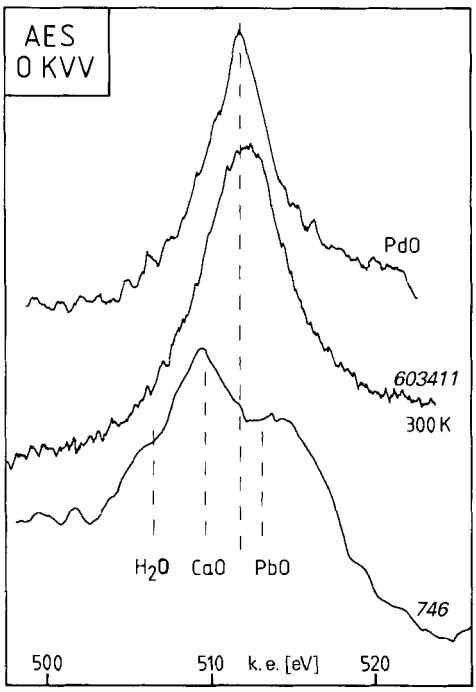

Fig. 11. *X-Ray-induced* Auger *spectra of the reference compound PdO, the experimental catalyst after the first heat treatment* (603411) *and the industrial catalyst* 746. All spectra were recorded at room temperature. The broken lines for reference shifts are labelled with only approximate chemical identifications (see text).

The spectrum of the experimental catalyst is quite different from the industrial ones (*746* and *746*+ are almost identical). The spectrum of *746* exhibits most of its intensity in the range of H_2O and Ca compounds, *i.e.* of the free support. The spectrum of the experimental catalyst resembles that of PdO or Pd + O. Since in the thermal desorption experiment this catalyst evolved H_2 already at low temperatures (see *Fig. 7*), we conclude that its surface consists rather of $Pd(OH)_2$ than of PdO or Pd + O.

3.5.4. *Pd Spectra.* The transition metal Pd with an exceptional d^{10} ground-state configuration exhibits an intense core level and a characteristic valence-band spectrum. The 3d core levels were chosen for the investigation. They offer the advantage of the highest cross section, although their binding energies are close to those of the Ca 2p core levels. Satellite subtraction (to remove the Mg-$K\alpha_{3,4}$ satellites of the excitation source) in cases of intense Ca 2p spectra allows the undisturbed presentation of the Pd 3d core levels. The *Auger* transition involving the 3d core level and the valence band was also used to obtain chemical information about the Pd. No UPES data could be collected as consequence of the electrostatic charging. This as well as the XRD data exclude the presence of large metallic particles on the catalyst.

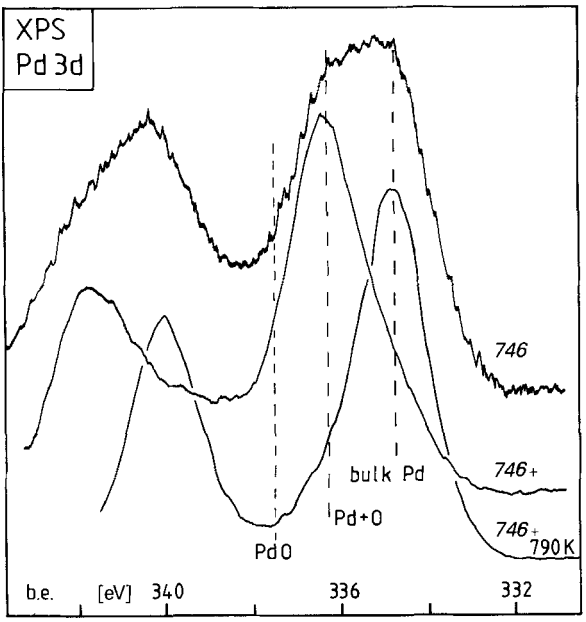

Fig. 12. *Pd 3d High-resolution spectra of the industrial catalysts.* The new batch was heated *in situ* to 790 K and yielded the bottom spectrum. Compare the magnitude of the heat-induced shift to that of the oxygen peak shown in *Fig. 10*. The broken lines are taken from measurements of the reference compounds in our apparatus under identical conditions of data acquisition.

In *Fig. 12*, we compare the Pd 3d spectra of the two batches of the industrial catalysts *746* and *746*+. The spectrum of the sample *746*+ after *in-situ* heating to 790 K is also shown. Reference lines for Pd foil, for the solid solution of oxygen in Pd, and for the divalent PdO are indicated. The observed b.e.'s are typical for zero-valent Pd. The solid solution of Pd + O is considered to be a zero-valent compound, since its structure is very

similar to the parent metal allowing significant Pd-Pd interaction. From its b.e. between that of Pd zero- and divalent Pd, this compound could be considered as a monovalent Pd species, similar to the one known for individual atoms in Pd-impregnated zeolite catalysts [16]. We note, however, that the line-shapes for *746* and *746+* are quite different. From comparison of the two spectra with the reference lines, we conclude that the spectrum of zero-valent Pd consists of two components which are present in equal amounts in the spectrum of *746* (line-width 4.0 eV FWHM). The spectrum of *746+* shows, at room temperature, predominantly the Pd + O component (line-width 2.48 eV), after heating to 790 K, predominantly the other Pd component (line-width 2.08 eV). The two batches of the catalyst differ only slightly in their catalytic activity, the sample *746+* being slightly better than *746*. This indicates that none of the two forms of zero-valent Pd is directly related to the catalytic performance. They represent a precursor state of the active species. We found, indeed, that the spectra of all catalysts used once are similar and contain again two zero-valent species, one of them being Pd + O (minority form) and the other being Pd with slightly higher b.e. than elemental bulk Pd.

It was found to be a typical feature of *Lindlar* catalysts to contain two types of zero-valent Pd in proportions varying greatly from sample to sample. It was already noted in the literature that the metallic Pd of *Lindlar* catalysts shows a strongly asymmetric Pd 3d core-level spectrum [5]. This asymmetry is much more pronounced than the one observed for metallic Pd (see *Fig. 13*) and results from the coupling of the core hole with the valence states (this effect is typical for all metallic systems) [17].

We have observed that the presence of divalent Pd is detrimental to the catalytic activity. Divalent Pd, as PdO, exhibits its $3d_{5/2}$ peak just in the valley between the spin-orbit doublet of elemental Pd and can be detected sensitively. All catalysts which had been made catalytically inactive by various treatments have in common a significant amount of divalent Pd.

The assignment of the species with a b.e. between that of bulk Pd and PdO to a solid solution of oxygen in Pd is supported by the large shift of 1.6 eV in the Pd 3d spectra of *746+* before and after thermal treatment. This shift cannot be ascribed to errors in the charge correction which is constant for all core levels. The corresponding O 1s spectra in *Fig. 10* differ only by 0.4 eV after the thermal treatment. The desorbed oxygen was just detectable in the residual gas analysis by its peak at m/z 32. The phase Pd + O has already been described in [18]. It was found during analysis of electrochemically oxidized Pd foil [19]. Our spectral parameters are in good agreement with the values quoted in this study.

The assignment of the species at lower b.e. is much more critical. From *Fig. 12*, one might conclude that this species is unambiguously metallic Pd. However, XRD analysis of the catalysts *746* and *746+* showed very little metallic Pd but rather a species with an enlarged lattice constant (see *Fig. 2*). After the heat treatment of sample *746+*, the diffractogram was so different from the precursor (loss of aragonite, change in line-shape for calcite) that the reflections for Pd could not be identified. We have no indication which of the two XPES peaks is correlated with the XRD. Since XRD requires a certain degree of crystallinity, whereas XPES does not, it is not clear whether XRD and XPES are correlated at all. Thus, the assignment of the low b.e. XPES feature to elemental Pd needs some further critical examination.

We observed during the analysis of a wide series of *Lindlar* catalysts that the b.e. of the metallic Pd is not constant but varies by about 0.8 eV between 334.7 eV and 335.5 eV.

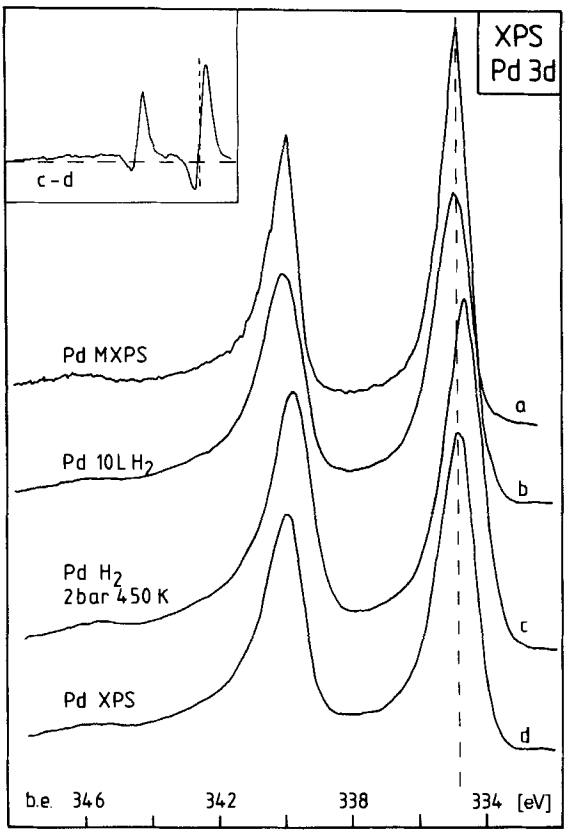

Fig. 13. *Pd 3d High-resolution spectra of elemental Pd under different conditions.* The top spectrum (*a*) was taken with monochromatic Al-*Kα* excitation to show the true line-shape of the photo-emission peaks. This spectrum should be compared to the conventional spectrum taken in our apparatus (trace *d*), note the excellent agreement in the positions. The central spectra show the effect of H_2 treatment on these core levels. Trace *b* after chemisorption of 10 L H_2, trace *c* after loading the same Pd foil with H_2 in a high-pressure chamber attached to the spectrometer. The inset shows the difference spectrum to pure Pd. Note the shift and the changed cross section. The ordinate of the inset is expanded by a factor of 5 relative to the main figure. All spectra were recorded at room temperature.

Pure metallic Pd can also not be distinguished from α-PdH and exhibits only a small shift of *ca.* 0.2 eV (FWHM for clean and H_2-exposed Pd 1.47 eV), if it is converted to the β-Pd-H. The existence of the hydrides in the reference samples was verified by the corresponding He(II)-UPES spectra (see also *Sect. 4.1.4*) which were very similar to the data in [20]. Distinction between α- and β-PdH was made by thermal desorption after the spectra had been measured. We show this situation for polycrystalline Pd foils in *Fig. 13*. For comparison, the spectrum of the clean foil was also measured with monochromator XPES on a *Leybold Hereaus LHS 11* instrument[3]). The reproducibility of the b.e. was excellent as can be seen in *Fig. 13*. The line-width decreased to 1.07 eV. The asymmetry of the peaks due to coupling of the core hole with the valence band is clearly visible. We note that the satellite of the Pd $3d_{3/2}$ core level which shows up in the left of *Fig. 13* as a weak

[3]) We thank Dr. *Oelhafen*, Institute of Physics, University of Basle, for the spectrum.

structure is insensitive to the presence of hydrogen in the lattice of Pd. The cross section for photo-emission is larger for the hydride than for the pure element as can be seen from the difference spectrum displayed in the inset of *Fig. 13*.

The detailed interpretation of the spectrum of the metallic Pd is further complicated by the relaxation shift induced by the small particle size. It is known that the valence-band spectra and the core level b.e.'s of small metal particles start to change at particle sizes below *ca.* 5 nm [21]. At this particle size, the Pd 4d conduction band starts to shift gradually to higher b.e. The characteristic valence-band spectrum with the huge *Fermi* edge starts to transform into a narrow 4d peak associated with a continuous loss of the *Fermi* edge feature. We note that the Pd + O phase gives also rise to a d-band shift of 1.9 eV relative to bulk Pd.

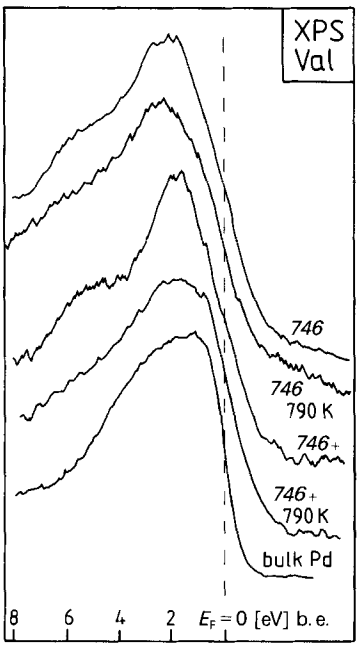

Fig. 14. Valence-band spectra of the industrial catalysts before and after *in-situ* heat treatment excited with Mg-$K\alpha$ radiation. The reference spectrum of Pd foil is 50 times more intense than the spectra of the catalysts (acquisition time typically 10 h). All spectra are dominated by the Pd 4d band.

In *Fig. 14*, the XPES valence-band spectra of the two industrial catalysts at room temperature and at 790 K are compared with the spectrum of bulk Pd at room temperature. The latter spectrum is *ca.* 50 times more intense than the spectra of the catalysts (see also *Fig. 8*).

Both catalysts exhibit at room temperature a narrow d-band feature distinctly different from bulk Pd. Only a part of the slope at zero energy may be ascribed to a *Fermi* edge. A clear distinction between a *Fermi* edge and any other density of states near zero energy is not possible due to the limited resolution of XPES valence-band data. In both spectra, the d-band maximum is shifted to higher b.e. (1.9 eV for *746*+ and 2.4 eV for *746*). The structure around 5.5 eV arises from 2p states of O associated with Pd. These states in H_2O

or $CaCO_3$ give hardly rise to any appreciable structure in the XPES valence-band spectrum. This is in line with the general rule that π-symmetry type states exhibit low cross sections in the XPES experiment [17]. We observed in PdO a sharp peak at 5.9 eV completely separated from the narrow d band. The broad feature seen in *Fig. 14* is typical for O in Pd in a subsurface bound state, *i.e.*, for the solid solution state. This was also verified by He(II) UPES data taken from a pure sample of Pd + O.

This interpretation is further substantiated by the high-temperature spectra shown in *Fig. 14*. In both catalysts, the intensity of the oxygen feature is drastically reduced after heating to 790 K *in situ* (compare with the transformation in the Pd 3d spectra shown in *Fig. 12*). The overall line-shape changes as well and the d-band shift is reduced. Heating causes the catalysts to loose the Pd + O phase (loss of the O 2π states). The Pd transforms into a state similar to the bulk elemental state. This may be effected by either the loss of the hydride (all samples lost H_2 at 790 K) or by coagulation of small particles to form larger aggregates or a combination of both effects.

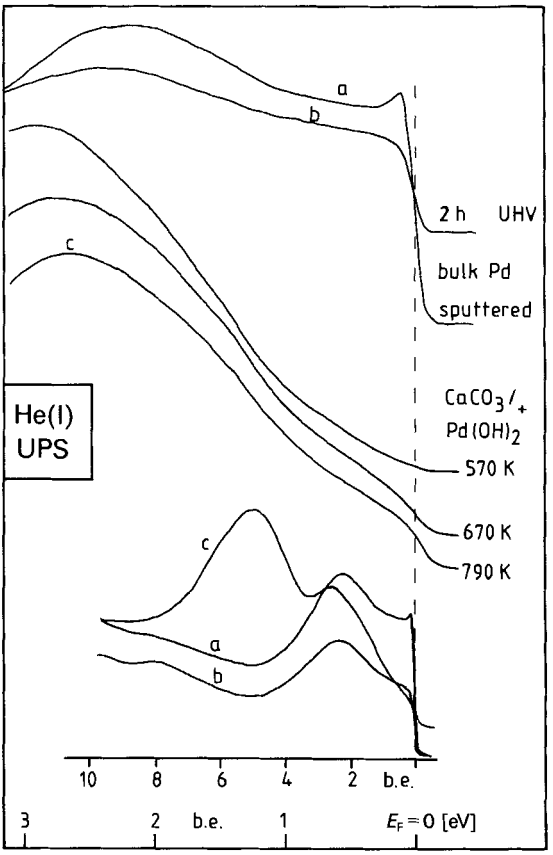

Fig. 15. Top: *Expanded UPES spectra of the conduction bands of Pd foil freshly sputtered* (*a*) *and stored after sputtering in UHV* (*b*), *as reference to the experimental catalyst* (*c*). Before the *in-situ* heat treatment indicated in the figure the material was already heated to 650 K (see *Sect. 2*). The intensity scales are equal for all traces. The inset (bottom, note the different energy scale) shows the differences of the three surfaces (the experimental catalyst (*c*) at 790 K, the Pd foil at room temperature) in the deeper-lying energy states. The main peak in *c* arises from O 2p states.

The valence-band spectra offer the explanation for the variation in the b.e. of the 'metallic' Pd 3d subspectrum. The shape of the Pd d-band gives evidence for the presence of small particles of Pd of a size which is just at the onset of the critical size for relaxation phenomena to become relevant. This gives an estimate of *ca.* 5 nm for the Pd particles which would be undetectable by XRD in abundance of below 5 wt.-%. Any presence of the β-PdH would be impossible to recognise by the Pd 3d shift against the floating reference of elemental Pd present as small particles (see *Fig. 13*). In summary, the nature of the zero-valent species which exists besides the solid solution Pd + O cannot be elucidated from XPES alone. The size of 5 nm is about the lower limit where formation of the hydride phase is known to occur [22]. This second Pd species may well be in the form of fully or partially H-loaded small particles.

The special properties of small Pd particles on $CaCO_3$ have been established in experiments with the experimental catalyst. Due to the complete coverage of the calcite surface with Pd, there was no charging, and it was, therefore, possible to record UPES data. In *Fig. 15,* He(I) spectra of sputtered Pd foil are compared with those from the experimental catalyst heated *in situ*. The parallel shift of the Pd 3d core levels confirms that this high-temperature treatment caused the $Pd(OH)_2$ to transform into a metallic species.

The top trace *'a'* in *Fig. 15* arises from the clean surface of a polycrystalline Pd foil without thermal annealing and trace *'b'* represents a state where some CO from the residual gas has been adsorbed. The adsorbed species reduced the height of the *Fermi* edge drastically (intensity normalized to a data point at 3.1 eV). The CO was directly identified in the corresponding He(II) spectrum. The compressed scale presentation in the lower part of *Fig. 15* shows very little effect of this adsorption on the other main features of the spectrum.

Up to a temperature of 570 K, the surface of the experimental catalyst consisted of $Pd(OH)_2$ (no intensity at zero energy). At 670 K, the transformation to a metallic state is in progress (according to XPES 30% zero-valent, 70% divalent), and at 790 K all the divalent Pd has reacted to a mixture of Pd + O and the zero-valent species with the same b.e. as found for the industrial catalysts. The comparison of traces *'a'* and *'c'* in *Fig. 15* clearly shows that this zero-valent species is not of bulk metallic character. This holds even under the assumption that an adsorbed layer on top of the Pd was formed (compare traces *'b'* and *'c'*). Note the d-band shift which is visible in the expanded scale presentation as well as in the compressed scale spectra which show the O 2p states to be the most intense feature. This is expected for a π-symmetry type state in the He(I) experiment (note the contrast to the XPES experiment, see *Fig. 14*).

The intensity at zero-energy is so small that it is difficult to assign, only from the shape of this feature, a metallic character with a *Fermi* edge to this state. This interpretation is strongly supported, however, by the simultaneous recording of the work function as detected by the low-energy cut-off of the secondary electrons in the He(I) spectrum. In *Fig. 16,* we show the change of the work function of the surface of the experimental catalyst with temperature. At the same temperature where the feature at zero energy starts to develop, one observes a sudden rise of the work function up to a value which is characteristic for Pd foil. The changes of the work function for different states of the surface of the polycrystalline sample are so large that these values can not serve as a standard to determine the expected influence of particle size on the work function. The

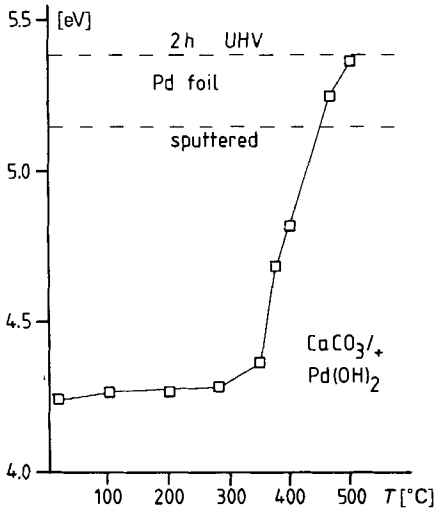

Fig. 16. *Evolution of the work function of the experimental catalyst surface during* in-situ *heating* (compare *Fig. 15*). The work function was taken from the cut-off of the low energy end of the He(I) spectra. The dashed lines are reference values from the Pd foil (*a, b* in *Fig. 15*) determined with the same method.

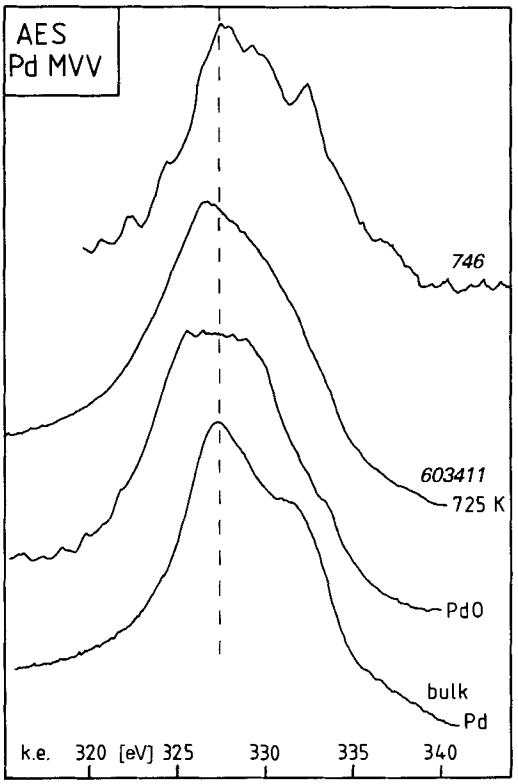

Fig. 17. *X-Ray-induced Pd* Auger *spectra of the industrial catalyst* 746 *at room temperature, of the experimental catalyst at 790 K* (after the first activation treatment at 650 K, see *Sect. 2.1*), *and of reference compounds PdO and Pd foil*. The spectrum of *746* is 15 times less intense than the other spectra shown in the same intensity scale.

increase in work function during storage in UHV, which was associated with the adsorption of a submonolayer quantity of CO, indicates the influence of structural relaxation on the work function after the sputtering process. The values given in *Fig. 16* should thus be taken merely as a trend rather than as accurate measurements.

The Pd MVV *Auger* transition was also used to obtain chemical information. In *Fig. 17*, the main part of this transition is shown for the catalyst *746*, the experimental catalyst at high temperature (*603411*) and for the reference materials PdO and Pd foil. We have observed that only very subtle changes of the line-shape occur in the spectrum of the bulk Pd upon loading with hydrogen and that the solid solution Pd + O exhibits a spectrum very similar in shape to that of PdO. Comparison of the reference spectra established the sensitivity of the shape of this *Auger* transition upon chemical state. It is thought to arise from the convolution of the *Fermi* edge into the transition, any shift of the spectrum is difficult to detect.

The spectra of the catalysts are of similar shape. The difference in the quality of the spectra is due to the different abundances of Pd on the surface of the two catalysts (the spectrum of *746* was accumulated for 24 h). They both establish more clearly than the valence-band spectra that bulk Pd metal can only be present as a small part of the Pd loading. Their shape can be reproduced by a superposition of the spectra of the reference compounds (PdO + bulk Pd). This is in line with the observation of the two species in the Pd 3d core level spectra.

3.5.5. *Pb Spectra.* The Pb 4f spectra were used (highest relative cross section) for the determination of the chemical state of the Pb additive. In *Fig. 18*, the spectra of the two industrial catalysts and of the heat-treated sample *746+* are compared. Reference compounds were the ingredient $PbCO_3$ as identified by XRD, a sample of calcite impregnated with $PbCO_3$, and a Pb foil. This foil yielded in its pure form (cleanliness checked with He(I) and He(II) UPES) a b.e. of 136.3 eV which is in good agreement with the literature value of 136.3–136.6 eV [23]. $Pb(AcO)_2$ and $PbCO_3$ exhibit the same b.e. of 138.7 eV (*Table 2*). Since $Pb(AcO)_2$ was not stable in the UHV (loss of H_2O and hydrolysis products, *e.g.* AcOH) it may have been decomposed to the carbonate. In the following, we refer to the carbonate standard, since its chemical nature under XPES conditions is far better defined.

The spectra of the Pb species of the two catalysts at room temperature are quite different. Heating *746+* causes its Pb 4f spectrum to transform into one very similar to that of *746*. The fact that this difference in chemical state of the Pb additive in *746* and untreated *746+* is not reflected in the catalytic activity indicates that the majority of this Pb is merely a spectator species and not related to the operation of the catalyst. This is supported by the observation that the surface concentration of Pb measured in a large series of catalysts did not correlate with the relative catalytic activity nor selectivity [24].

The spectrum of *746* exhibits its maximum intensity at a b.e. (136.8 eV) which is typical for zero-valent Pb. The same b.e. was obtained for the thermally decomposed $PbCO_3/CaCO_3$ system. PbO, a likely candidate for these species, exhibits a b.e. of 137.3 eV close to the value for the starting compound (see *Table 2*). We noted that $PbCO_3$ precipitated on $CaCO_3$ showed a distinctly lower b.e. than pure $PbCO_3$ and was probably transformed to $Pb(OH)_2$.

The spectrum of the catalyst *746* is asymmetric to lower b.e. indicating the presence of a second zero-valent species. A small amount of zero-valent Pb is present also in the

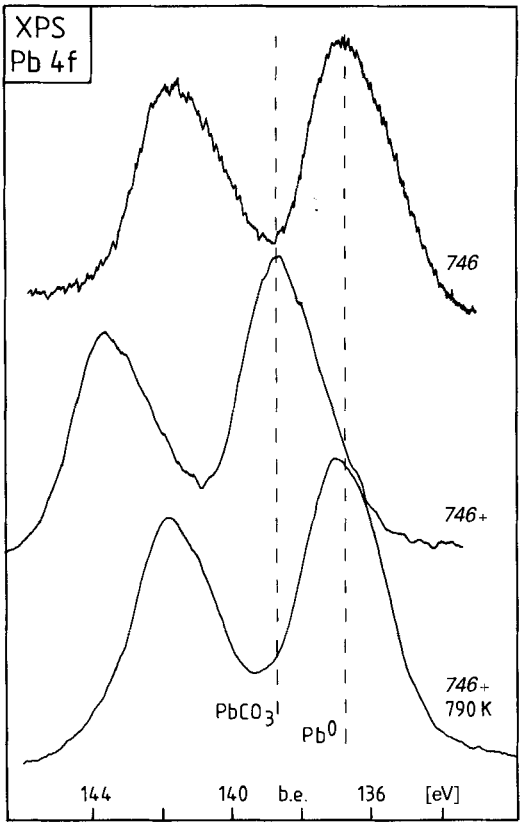

Fig. 18. *Pb 4f High-resolution spectra of the industrial catalysts.* The new batch was heated *in situ* to 790 K. The broken lines were taken from reference compounds measured under identical conditions of data acquisition.

sample *746*+ at room temperature. Heating caused the $PbCO_3$ to decompose and, thus, the spectrum to shift with the majority of its intensity to the position of the main zero-valent Pb peak.

The ratio between zero-valent and divalent Pb was not constant for different samples of the catalyst *746*. Several specimen from the same batch were similar in total content of Pb and Pd, but the ratio between zero- and divalent Pb compounds varied considerably. The divalent species was not present as carbonate, but showed the same b.e. as in the model lead-calcium carbonate, *i.e.* it was present as hydroxide.

It is interesting to note the predominantly zero-valent character of Pb in this (aged) sample, whereas the freshly prepared catalyst *746*+ contains Pb predominantly in the divalent form in agreement with the preparation. No reduction step was performed after the precipitation of the $Pb(AcO)_2$. We conclude that a large fraction of the divalent Pb was reduced in a slow process after the manufacture of the catalyst was terminated. This reduction may have occurred by H transfer from adjacent Pd particles. As stated before, the majority of the Pd may be present as PdH and, thus, be able to reduce these fractions of the Pb which are close to the Pd particles.

The Pb spectra of all used catalysts were very similar and showed a predominant peak at the position for $Pb(OH)_2$ and a small peak typical for zero-valent Pb. This peak was in all used samples of the catalyst *746* considerably smaller than for the unused catalyst. All active catalysts had, on the other hand, at least a small trace of zero-valent Pb.

The nature of this zero-valent Pb which seems to be related to the catalytic action could not be further evaluated, since chemical shifts between Pb metal and Pd-rich Pb-Pd alloys are too small to be of diagnostic value. Contrary to bulk Pb which was rather insensitive to chemisorption, the Pb species on both the heated *746* + sample and on the model carbonate system were sensitive to contamination. Initially the peaks were less asymmetric and centered at the low b.e. shoulder of the spectrum shown in *Fig. 18*. After *ca.* 30 min in UHV, the spectra had changed to the shape displayed in *Fig. 18, i.e.* the low-b.e. species disappeared gradually. A chemical reaction such as uptake of O_2 without oxidation could have immobilized the zero-valent Pb. At 790 K, bulk Pb is liquid but no indication of visible vaporisation of Pb or segregation of metallic Pb as droplets (in the optical microscope) from the catalyst sample was detected.

3.5.6. *Quantitative Determination of the Surface Composition.* The results of the quantification of the core-level spectra using empirical cross section values [11] for the elements are compiled in *Table 3*. Although the nominal accuracy of the numbers is about 1%, the quantitative relevance of these results is limited. The sample surfaces contain at least seven different chemical species, and they are inhomogeneously charged. This makes the assumption of an universal information depth and peak areas solely related to elemental concentrations doubtful. Nevertheless some general trends can be seen in the data of *Table 3* which will be briefly discussed.

Table 3. *Surface Composition of Some Catalysts.* All values in at.-%.

Sample	O	C	Ca	Pd	Pb	Cl
746	55.2	31.5	7.1	3.6	2.6	–
746+	56.3	26.5	11.1	2.0	3.2	0.9
603411	47[a])	10.1	–	34.0	–	8.9
603411 (790 K)	23[a])	19.9	5.3	51.0	–	0.8
746+ (790 K)	51.4	31.6	11.9	1.6	3.3	0.2

[a]) Due to overlap of O 1s with Pd $3p_{3/2}$, only graphical estimates. Errors are larger than last decimal, which is, however, given to account for the small surface components.

The abundance of O compared to the one of Ca is far too large to be accounted for by $CaCO_3$. This holds also for C. Other O-rich compounds have to be present. The lack of lateral resolution of XPES does not permit to decide, whether the other compounds form a thin overlayer (*e.g.* as contamination film) or islands on the surface of the carbonate carrier.

The industrial catalysts contain the active metals in low dispersion as follows from the comparison of the bulk analytical content of *ca.* 5 wt.-% Pd (= 4.7 at.-%) and the abundance at the surface (see *Table 3*). The dispersion *D* is defined as the ratio of active atoms exposed at the surface to the total number of active atoms in the catalyst. The bulk analytical content of Pb is 4 wt.-% (= 1.9 at.-%). The atomic ratio Pb/Pd is 1:2.4. The differences in the surface contents indicate once more that the two metals are present in several chemical species which are not related to each other. Heating the catalyst *746*+

caused the Pd to agglomerate, whereas the Pb stayed almost unchanged in abundance. Only small amounts of Cl impurities were detected for the catalyst *746+*. Heating reduced its amount further.

The experimental catalyst exhibits, in contrast to the chemically reduced industrial catalysts, a surface of $Pd(OH)_2$ in the 'as precipitated' state and a Pd surface after heating. This high dispersion reduced the electrostatic charging in the XPES experiments to values below 1.0 eV and allowed the observation of UPES data. We note the large content of Cl in the surface of the catalyst before, and the drastic reduction of the Cl content after thermal activation. The Pd dispersion was not reduced by the heat treatment and by the loss of Cl. We conclude that the Cl is not involved in the anchoring of the metal on the support surface. The catalyst proved to be very active in reaction tests but the selectivity was very poor. This underlines the separation of good catalytic performance in the hydrogenation activity on the one hand controlled by the Pd surface content, and the product selectivity on the other hand controlled by the presence of an appropriate species of Pb (very little lead as hydroxide was found on the surface of the activated experimental catalyst).

The data in *Table 3* have been obtained with an emission angle of 90°. To check for the possible enrichment of one component on the top surface of the samples from the industrial catalysts, we varied the angle of emission between 90° and 45°. (It was shown by *Baird et al.* that effects of surface enrichment can be detected even on rough samples by variing the emission angle [25].) No change in the Pd/Pb ratio was observed. The Pd/Ca ratio varies slightly with the angle of emission indicating the influence of the rough surface and shadowing effects. The small abundance of Ca on the surface of the experimental catalyst vanished completely at 45° emission-angle. The Pd seems to be present in individual particles with small gaps in between which disappear in the shadow of the Pd particles at small emission angles.

The possible enrichment of Pb on Pd which was suspected in the literature to account for the selectivity of the catalyst was studied with the sample *746* using He ISS which samples only the top atomic layer of the surface. The reference alloy $Pd_{90}Pb_{10}$ was used to calibrate the cross sections for the Pd and Pb peaks of the ISS data. The polycrystalline and rough surface of the catalyst sample resulted in very broad low-energy parts of the spectra containing scattering from the support lattice. We found conditions under which the Pd and the Pb peak were as narrow as in the alloy (*ca.* 35 eV wide) and we were able to deduce the elemental ratio (Pd/Pb) on the catalyst surface. It was found to be 1.4 at room temperature which is exactly the same value as for the ratio obtained by XPES (1.4, see *Table 3*). There is no indication of a Pb overlayer over the Pd particles, if one accepts the assumption that the multiphase nature of the catalyst surface affects both ISS and XPES in the same way.

The Pd/Pb ratio is not stable when the temperature of the sample is changed. Upon heating, the ratio changes from 1.4 at 300 K to 2.21 at 400 K, and goes back to 1.6 at 520 K. At this temperature, where we observe the first weight loss in the TG experiment (at *ca.* 500 K, see *Fig. 6*), the ISS spectrum for Pd vanishes completely. The Pd signal reappears, however, after cooling to below 500 K for *ca.* 1 h. The ratio Pd/Pb is then 1.6 and stays at that value down to room temperature. The desorbed H_2O (see *Sect. 3.4*) is believed to cover the Pd particles at high temperature. The irreversible changes in the ratio Pd/Pb (the observed changes occur only during the first heating cycle, the ratio is constant in a

second heating experiment) indicate a rearrangement of the Pb-atoms on the Pd surface at temperatures which are lower than the decomposition temperatures of Pb compounds. The reference alloy showed a constant element ratio up to 500 K and was very little sensitive to sputtering. The composition of the top atom layer of the Pd-Pb alloy seems, thus, to be more stable than the one of the particles on the catalyst. This may be accounted for either by the small particle size or by the simultaneous presence of O in the Pd.

The experiments would also allow to see whether the Pb is present as an adsorbed layer on the Pd particles. It is found that the Pb does not cover the surface as an overlayer, but may be present only on suitable adsorption sites with large separations. The local presence of the Pb would block certain sites on the Pd for catalytic activity. The relative weak interaction between Pd and adsorbed Pb could account for the ISS data and might explain the high sensitivity of these catalysts against elevated temperatures.

3.6. *Electron Microscopy.* Both SEM and TEM at various levels of resolution were used to study the morphology and the micro-organisation of this multiphase solid. Energy dispersive microanalysis (EDX) was used to correlate the morphology with chemical composition.

3.6.1. *Scanning Electron Microscopy.* An extensive SEM investigation accompanied the course of this study. The morphology of the industrial catalysts (*746*) was found to be very reproducible under different conditions (before and after use, before and after heat treatment) and is exemplified in *Fig. 19a*. The catalysts form hedgehog-like agglomerates of needles. Interdispersed are agglomerates of droplet-like Pd particles. Using the enhanced element contrast of backscattered images, one can identify heavy elements at the tips of many needles and much smaller particles clustered on the surface of the needles.

The experimental catalyst *(603411; Fig. 19b)* exhibits a morphology of compact cubic or rhombohedral particles of *ca.* 1 μ size. This morphology is typical for calcite. The whole surface is covered by a dense layer of spherical particles with a uniform size of *ca.* 10 nm. Because of its shape this catalyst could not be studied with TEM.

High-resolution SEM carried out with uncoated specimen and 200 kV acceleration voltage revealed that the needles of the industrial catalysts are themselves aggregates of small microcrystals. The small particles adherent to the needles are also composed of several particulates which are often cubic in shape. These two details are exemplified in *Fig. 20*. The weak contrast results from the high acceleration voltage which was necessary to observe these nonconducting samples without any coating. Any coating could have given rise to artifacts at the high magnifications employed (250 000 in the primary image).

Using EDX, the following correlations between morphology and composition were established. The needles in the industrial catalysts are Ca compounds with very small amounts of Pd and Pb along their axes. The tips of the needles are formed by a Pb compound free of Ca. The agglomerates, not in contact with the support, consist of Pb-free Pd. We noted that most of the volume of the Pd loaded nominally onto the support is in fact not present in a form with intimate contact to the support, but forms a second phase of Pd only. This Pd is most probably lost for the catalytic activity, since it has been well established that both support and noble metal are needed to form a successful hydrogenation catalyst.

The small particulates on the experimental catalyst consist of Pd. In these samples, no support-free Pd was observed. It may be concluded that the Pd agglomerates on the

a)

b)

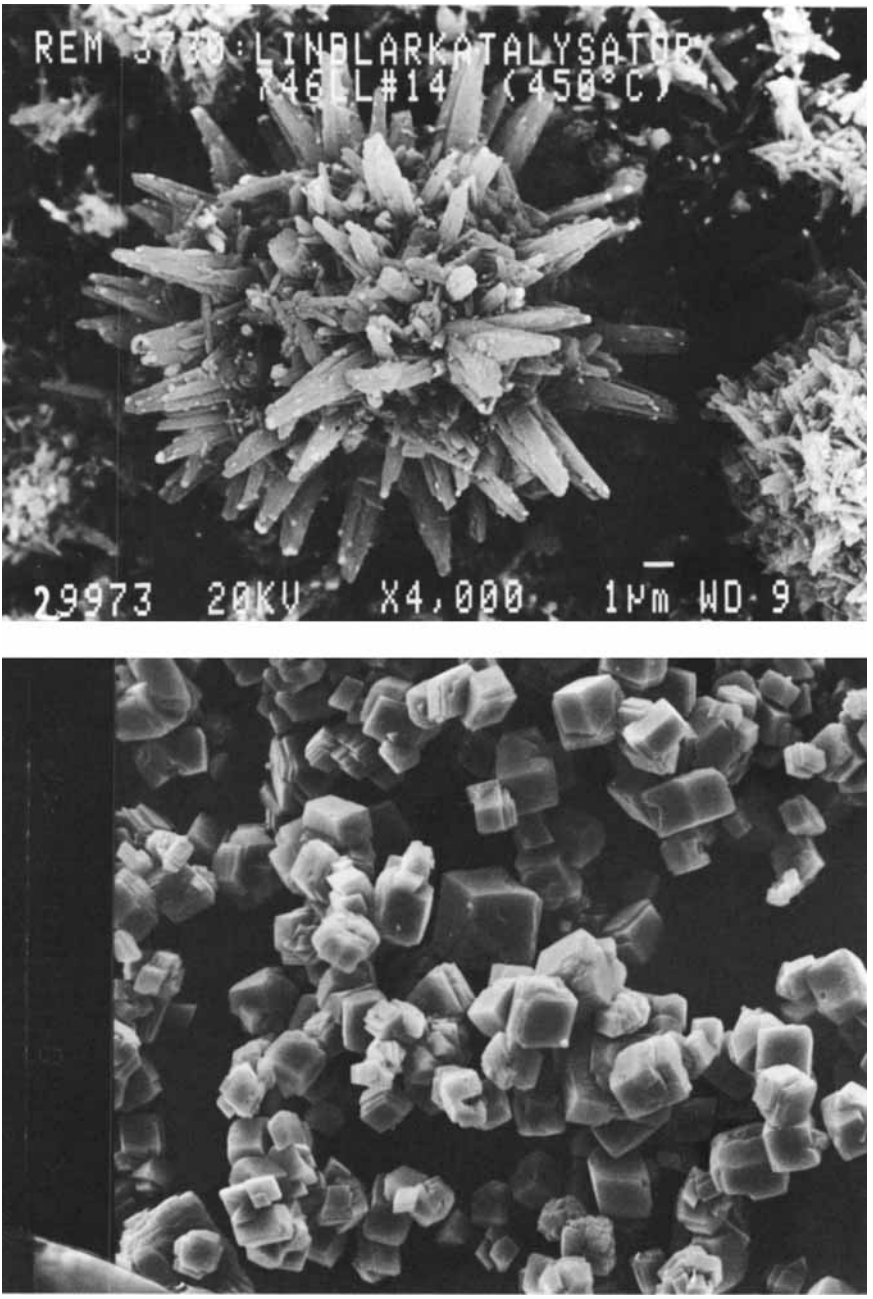

Fig. 19. a: *Typical SEM image of an industrial catalyst.* Images after one use, after heat treatment, and of the two batches were almost indistinguishable from the displayed one. EDX locates Pd and Pb within the complex agglomerate and shows that many of the tips of the needles contain significant amounts of Pb. The specimen was slightly gold coated. The acceleration voltage was 20 kV. b: *SEM Image of the experimental catalyst (603411), conditions as in* a.

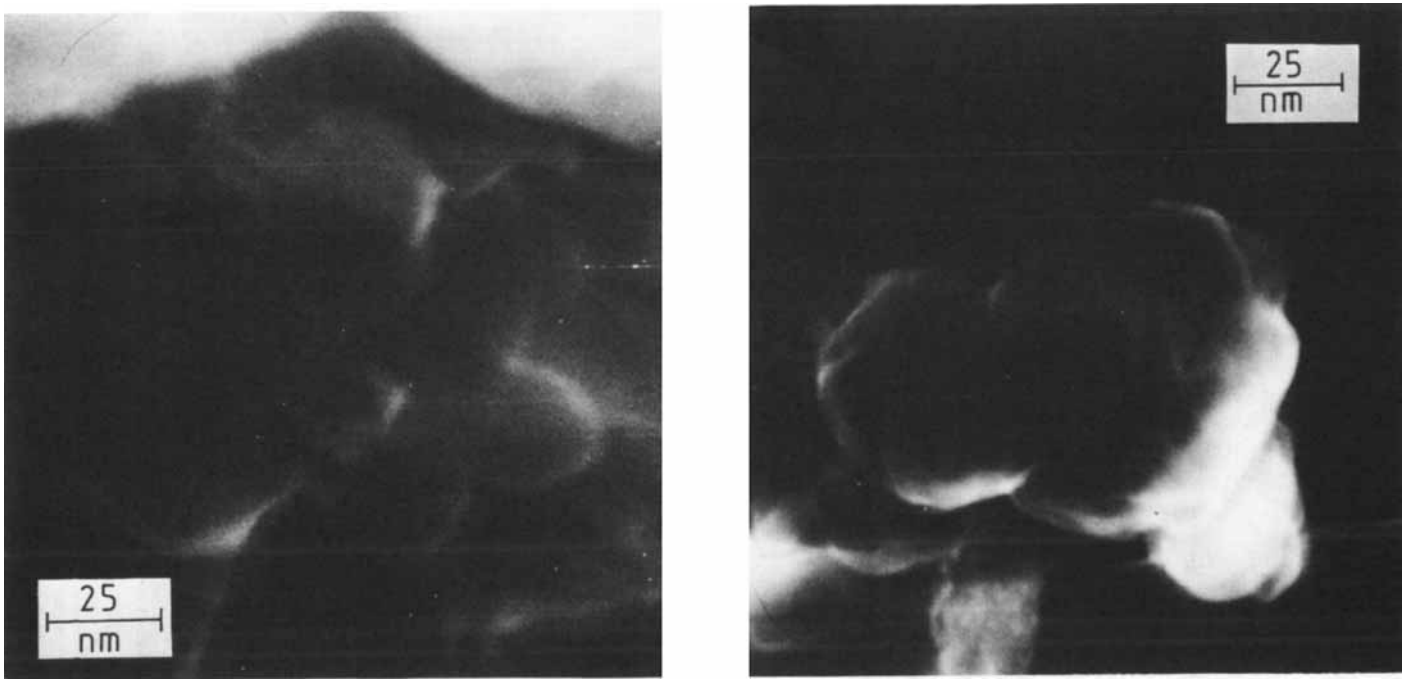

Fig. 20. *High-resolution SEM of the support and the Pd particles attached to it* (industrial catalyst *746*). The smooth needles of *Fig. 19* are clearly composed of small crystallites of $CaCO_3$. Note the spherical nature and the composition of a single Pd particle of several cubic (?) crystallites. The images were taken at 200-kV acceleration voltage without any coating of the nonconducting sample. This explains the low contrast.

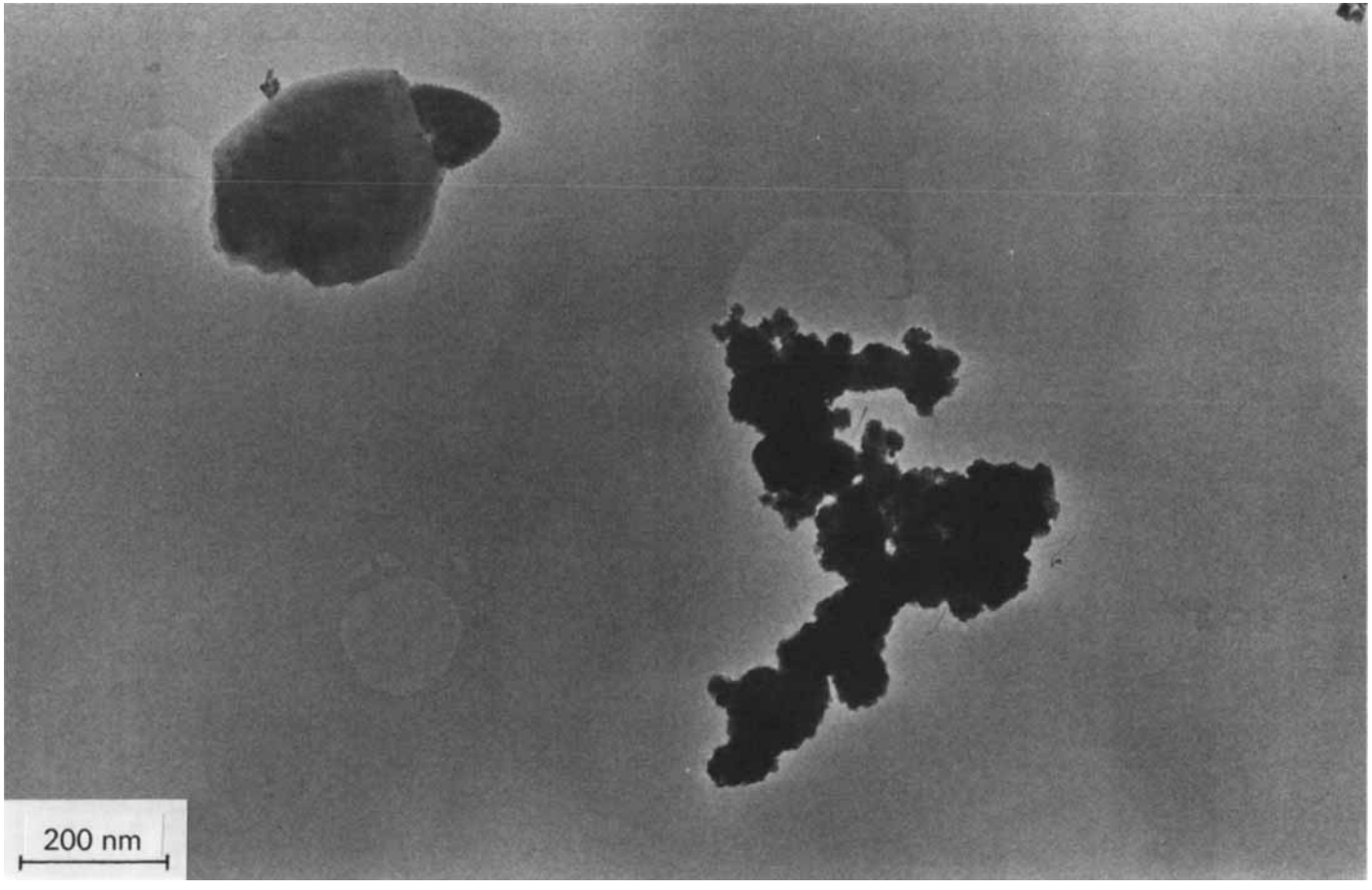

Fig. 21. *TEM Images of typical morphologies of catalyst particles* (*746*, top left) *and of Pd black* (right). The catalyst particle consists of two crystallites, the small tip-shaped particle is covered with Pd (dark spots). The Pd-black particle is an agglomerate of many disk-shaped Pd crystallites (see also *Fig. 25*).

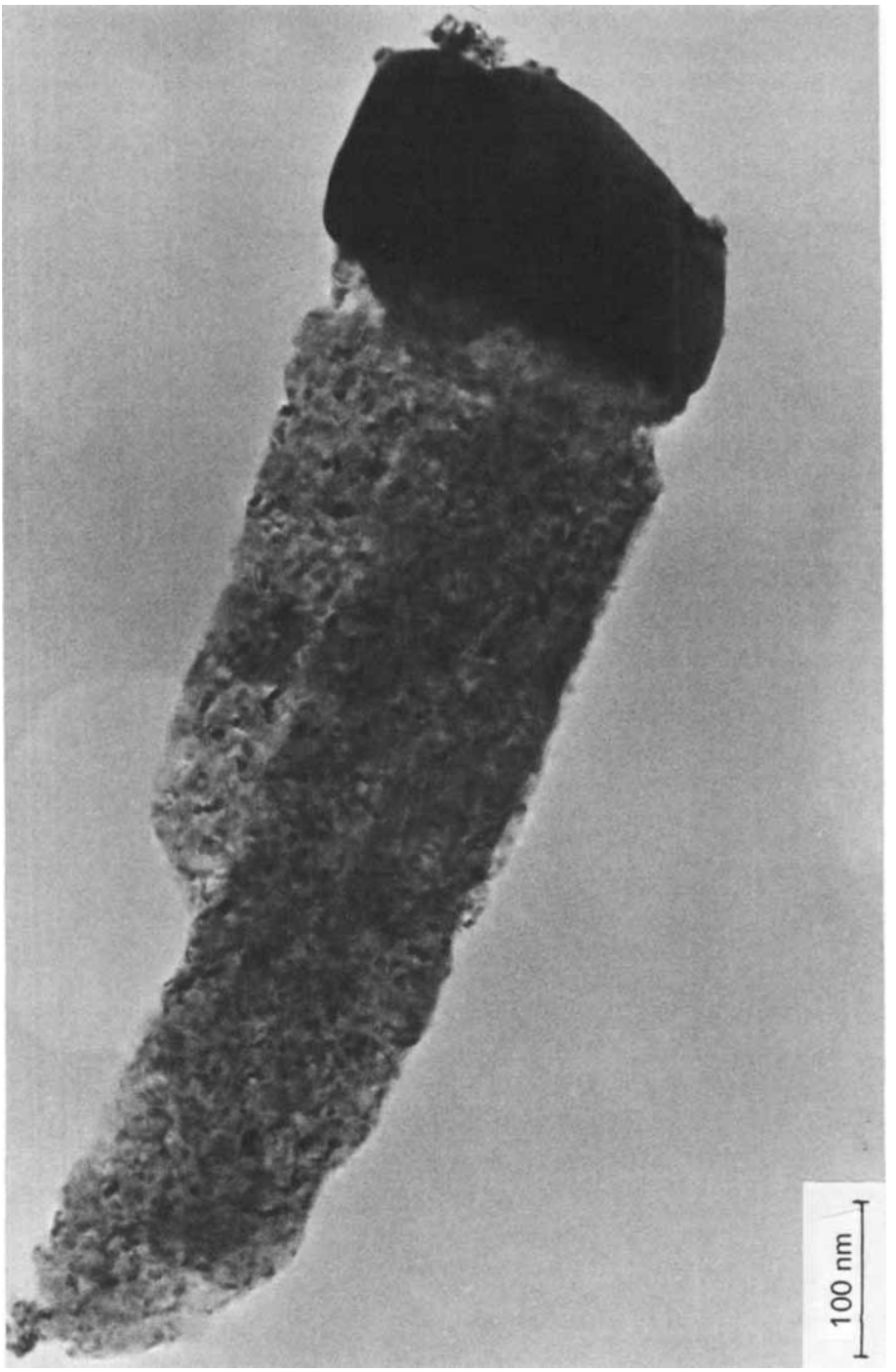

Fig. 22. *TEM of a single needle of the catalyst 746.* The microcrystalline nature of the needles is clearly visible, this particle is nearly free of Pd. The tip of the needle consists of a single crystal of $PbCO_3$.

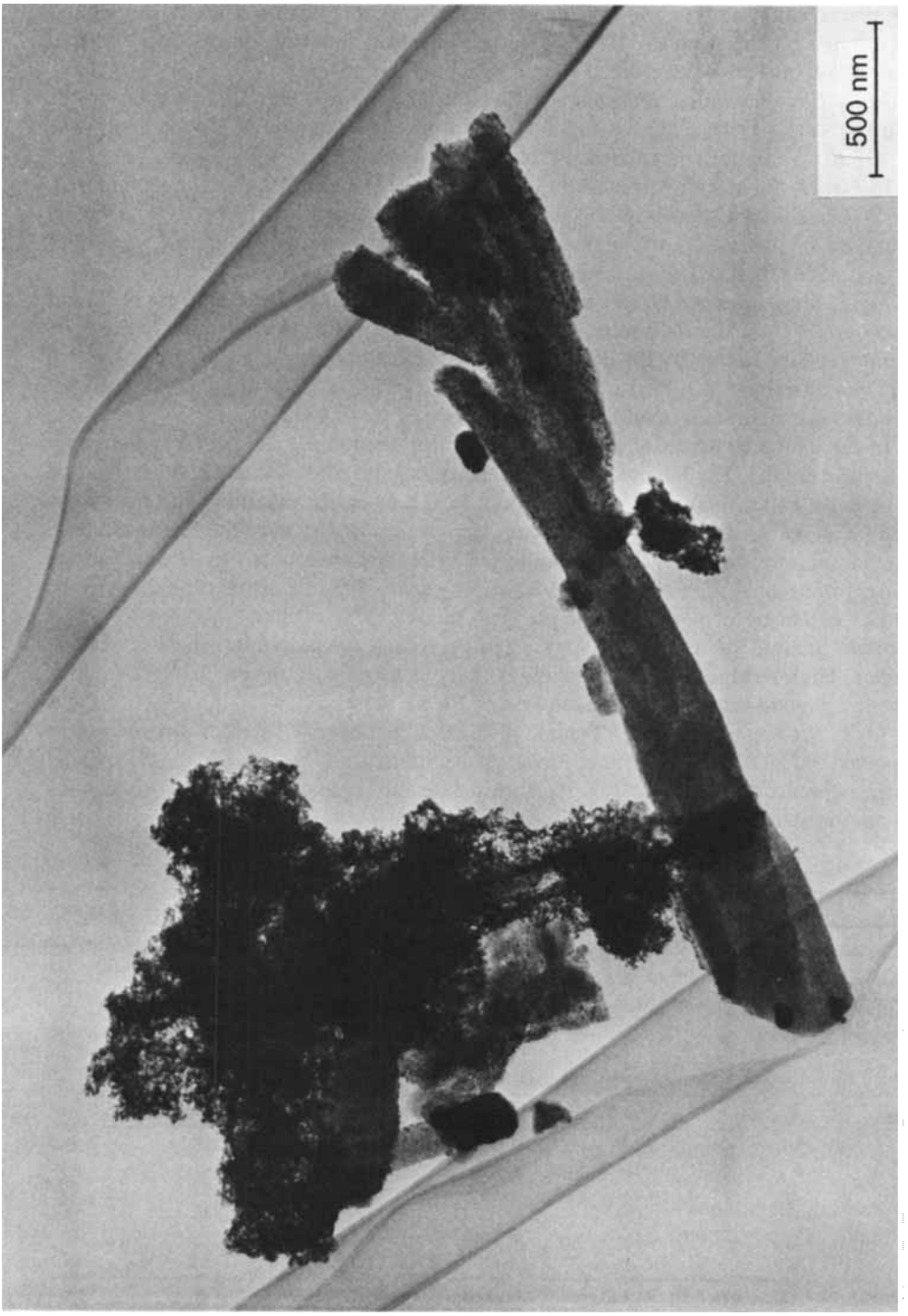

Fig. 23. *The industrial catalyst 746 contains besides the predominant needles also agglomerates of disk-shaped Pd particles which constitute a significant part of the total precious metal loading not attached to the support.* The Pd on the needles is visible as small dark spots.

commercial catalyst occur as consequence of the chemical reduction of the Pd compound precipitated on the support. We avoided this chemical reduction in our experimental catalyst and obtained, therefore, a system with high dispersion.

3.6.2. *Low-Resolution Transmission Electron Microscopy.* Only the samples of the industrial catalysts were thin enough for TEM work. The sample *746*, its precursor (5% *CE 407 R/D*) and, for comparison, Pd black were investigated.

In *Fig. 21*, the morphologies of the catalyst (top left) and of Pd black are compared. The Pd black is an agglomerate of small disk-shaped particulates. The catalyst particle is composed of two units, one of them being almost free of any precipitate, the other covered with very small objects consisting of Pd and traces of Pb.

Fig. 22 shows a more typical needle of the catalyst. The element contrast of the tip region arises from the Pb concentrated in this section. This needle exhibits clearly its microcrystalline nature by the detailed contrast. The corresponding diffraction pattern identifies this object as a mixture of calcite and aragonite without any Pd. The contrast thus does not arise from small Pd particles supported on $CaCO_3$.

In *Fig. 23*, we compare, at a lower magnification than in *Fig. 22*, the Pd agglomerate with some needles. The Pd looks similar to the aggregates of the Pd black, the individual particulates being thinner and smaller than in the reference material. The Pd on the support is visible as small dark spots on the surface of the needles. The distinction between support microparticles and Pd particles becomes obvious in *Fig. 24* which shows an array of needles. We note the irregular arrangement of the elemental crystallites in the needles which are of regular shape on their surface. This regular shape led to a first incorrect analysis of the morphology as being typical for aragonite single crystalline needles. High-resolution EDX confirmed that, in needles as shown in *Fig. 24* which contain adherent small particles, both Pd and Pb are present.

3.6.3. *Diffraction Patterns.* Typical diffraction patterns collected from objects as displayed in *Fig. 24* are compiled in *Fig. 25*. The pattern at the bottom of *Fig. 25* is typical for the reference material Pd black. Numerical data and the assignments of the reflections are summarised in *Table 4*.

Table 4. *Interpretation of Electron Diffraction Patterns*

Pd-Black Reference

Ring	Intensity	d Value [nm]	*JCPDS*[a]) *18-951*	*hkl*
1	*s*	0.2325	0.232	*111*
2	*m*	0.2010	0.201	*200*
3	*m*	0.1415	0.142	*220*
4	*m*	0.1201	0.121	*311*
5	*w*	0.0808	0.081	*422*

Catalyst Particle as in Fig. 24

Ring	Intensity	d Value [nm]	*JCPDS*[b]) *5-586*	*hkl*	*JCPDS*[c]) *5-453*	*hkl*
1	*s*	0.289	–	–	0.289	*002*
2	*s*	0.248	0.249	*110*		–
3	*m*	0.174		–	0.174	*113*
4	*w*	0.149	–	–	0.149	*241*
5	*w*	0.144	0.145	*300*	–	–
6	*w*	0.123	0.122	*1112*	–	–

[a]) β-PdH (Pd + O, see text; [12]). [b]) Calcite. [c]) Aragonite.

Fig. 24. *TEM Image of a group of needles in the catalyst 746.* The constitution of the well-shaped needles of many microcystals is clearly visible. These needles carry Pd particles (black spherical particles) of the type imaged in *Fig. 20.*

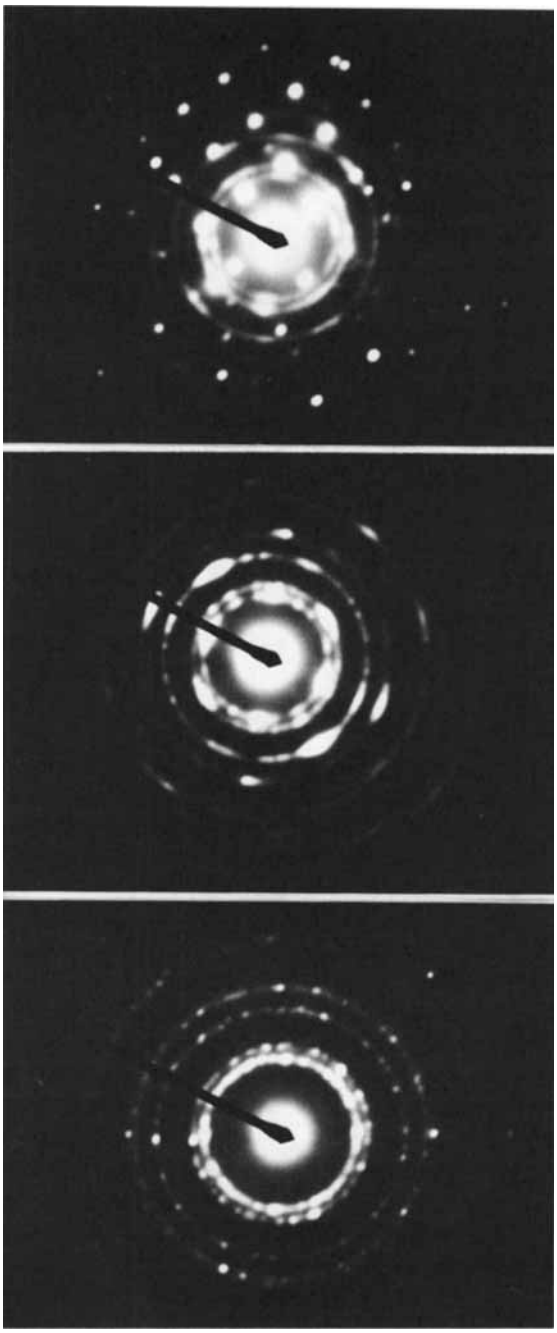

Fig. 25. *Typical diffraction patterns of* 746 (top two patterns) *and of Pd black* (bottom) *as reference.* This latter material consists of PdH or Pd + O and not of elemental Pd according to the diffraction pattern (see text). The two upper patterns are interpreted in *Figs. 26* and *27.*

The reference material consists of small particles in random orientation. The size of the microcrystals must be of the order of several nm. The d values clearly identify Pd black as β-Pd-H *(Table 4)*. Elemental Pd exhibits a similar pattern but starting with a d value of 2.25, which is smaller than the observed value of d = 2.32. This difference exceeds the experimental error.

The assignment of the diffraction pattern to β-PdH is only based on the enlarged d spacings. An XPES analysis of the reference material revealed that this Pd black consists in fact of Pd + O with about 30% elemental Pd or hydride (see *Sect. 3.5.4*). This is in line with the apparent stability in air which is unexpected for a hydride. The elemental Pd does not show up either in the electron diffraction pattern or in a conventional XRD trace. It seems to be present only at the surface of the sample. Thermogravimetry showed that only as little as 2 wt.-% O were dissolved in the Pd. It is interesting to note how O in a concentration of only 14 at.-% influences the ionic (enlargment of the lattice parameter) and electronic structure (see XPES data in *Sect. 3.5.4*) of Pd.

The most frequently observed diffraction pattern is displayed in the center of *Fig. 25*. At first glance, it is similar to the reference pattern, but exhibits clear signs of orientation of the ensemble of microcrystals. More accurate analysis reveals, however, that this pattern arises form a mixture of calcite and aragonite *(Table 4)*. The assignment is schematically shown in *Fig. 26*. The spotty ring diagrams give evidence for preferential orientation of calcite to aragonite as well as of two orientations of aragonite (see *Fig. 26*). The two orientations of aragonite are such that the *(110)* directions coincide. A possible explanation for this unusual relationship of two crystal structures with very different overall symmetry may be the following. Under the orientations given in *Fig. 26* the unit cells of calcite and aragonite are orientated such that layers of Ca ions are parallel. In the other direction, the mutual orientation is variable (ring diagram). This special crystallographic relationship could stabilize the many grain boundaries which are present in the needles. This stabilisation would then account for the low reactivity of this solid (interruption of the front of reaction) for the conversion of aragonite to calcite. This is expected to occur during impregnation of the support with the catalytic elements.

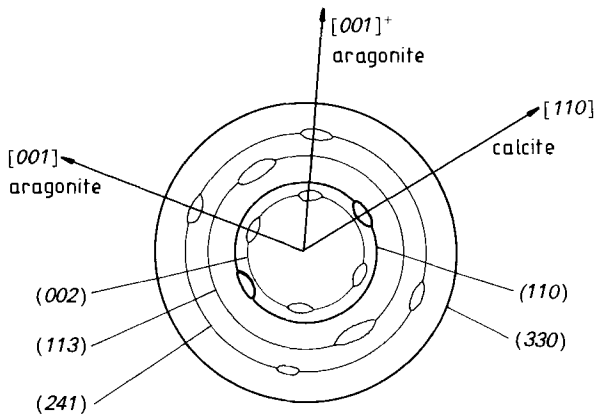

Fig. 26. *Interpretation of the central diffraction pattern of* Fig. 25. It represents a superposition of preferentially oriented microcrystals of calcite and aragonite. There is no strong indication for the presence of Pd (see text).

Reflections for Pd occur as extremely weak spots between the second and third ring at a d value of 2.01 (not visible in the reproduction shown in *Fig. 25*). We assign these weak spots to the (*200*) reflection of PdH or Pd + O (see above). The most intense reflection for this structure is (*111*) which would nearly coincide with the (*113*) reflection of calcite. It will, thus, be hidden under the second ring in the diffraction pattern. This finding is in line with the XRD observations shown in *Fig. 2*. The diffraction intensity from Pd was found to coincide exactly with the calcite (*113*) reflection.

Some spots in the rings of both aragonite and calcite indicate that some large domains of $CaCO_3$ are also present.

The diffraction pattern at the top of *Fig. 25* is a superposition of the ring diagram seen in the center of *Fig. 25* and a single-crystal pattern. This is schematically displayed in *Fig. 27* which gives also the lattice parameters and the identification of the single-crystalline phase. We observe the $Ca(OH)_2$ phase, already postulated from FTIR data and XPES core-level intensities, as thin crystals much larger than the supporting calcite and aragonite phases. Large parts of the surface of the support are covered with thin platelets of the hydroxide-carbonate phase. We note that this phase may have some structural relationship to calcite (see *Fig. 27*). A further topotactic relationship may be present. The lack of structural data for the hydroxide phase does not permit to further investigate this.

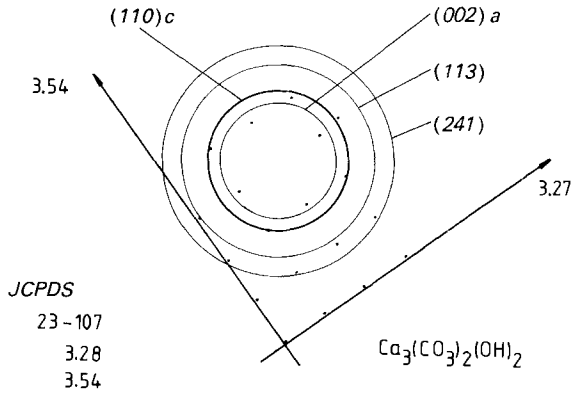

Fig. 27. *Interpretation of the top pattern of* Fig. 25. It represents the same superposition of calcite (*c*) and aragonite (*a*) as in *Fig. 26*. A comparatively large single crystal of calcium hydroxycarbonate causes the spotty pattern which allows the identification of the additional phase by the powder diffraction data file (*JCPDS*) [12].

Distinction between this phase and the monohydrate *(JCPDS 23-106)* is founded on the better agreement of the d spacings and on the observation of the stability of the specimen in the electron beam. Hydrates are expected to decompose under prolonged irradiation which was checked not to occur with our samples.

3.6.4. *High-Resolution TEM.* The analysis of the microstructure of the catalysts has shown this material to be a complex multiphase solid of largely microcrystalline nature. Lattice imaging should, thus, be capable to make the microstructure directly visible. We wish to point out that no difference in the images could be detected for specimens of the catalyst *746* and its precursor without Pb. We found no evidence for Pb to modify the Pd in any respect.

In *Fig. 28*, a small part of a needle is shown. We clearly can resolve a variety of lattice fringes. By variation of the focus condition, we were able to investigate most of the area

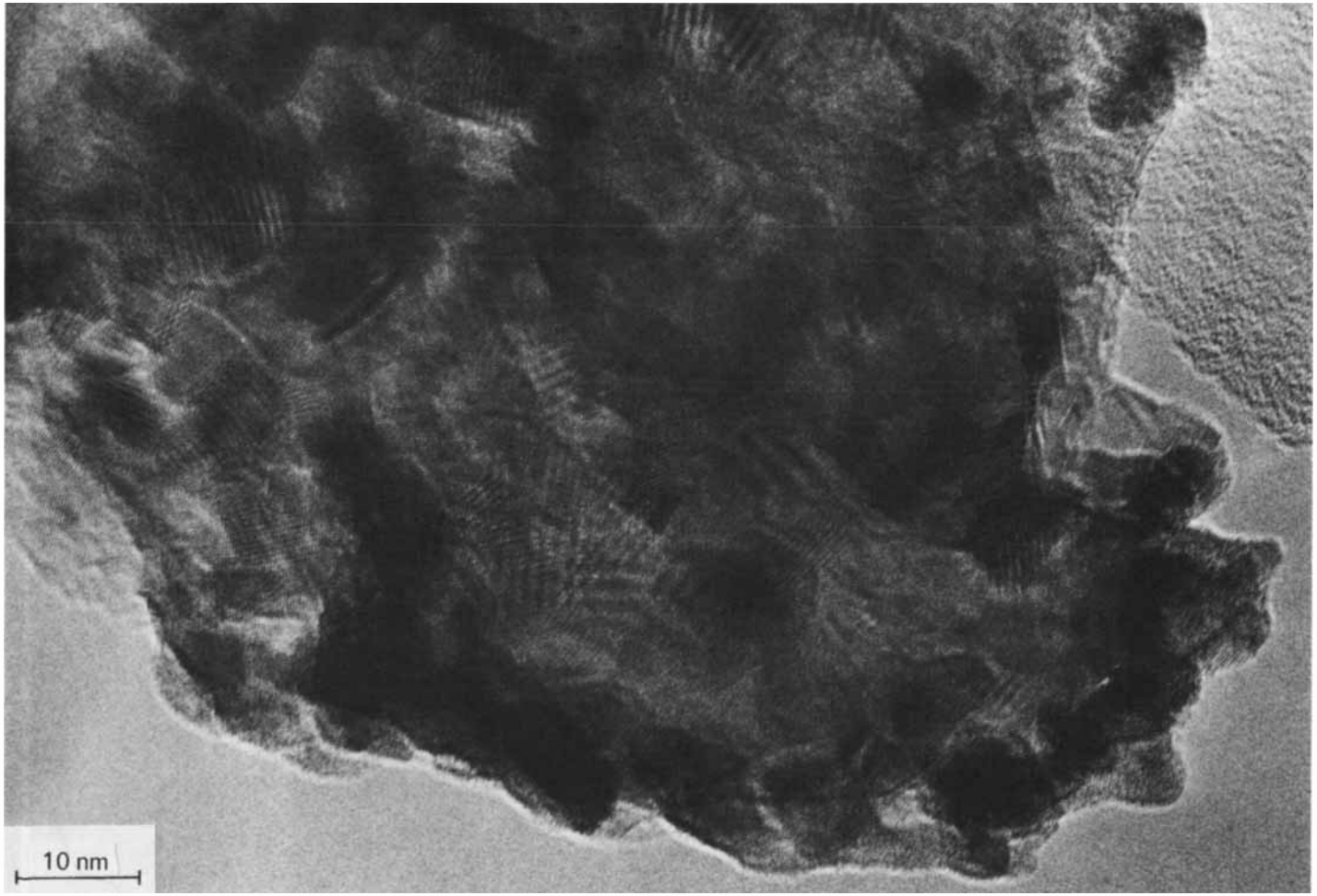

Fig. 28. *High-resolution TEM of a typical part of a needle as seen in* Figs. 20, 22–24. The large soft contours represent the individual crystallites of the needle. Well resolved lattice fringes allow the conclusion that these units consist of a set of microdomains of calcite and aragonite which are often intergrown under the angles showing up in the diffraction patterns as preferred orientations. There are few disk-shaped Pd islands present. These islands consist of lattice-expanded Pd and represent the Pd + O phase of the XPES data. In agreement with photo-emission data, only a small fraction of the surface of the support is covered with these particles.

displayed in *Fig. 28* (the object is of varying thickness). In *Fig. 29*, we have mapped out the various phases present in the viewing area. The microcrystalline nature of the catalyst is documented by the patchwork-like pattern. The Pd which is almost invisible in conventional images is present in thin disk shaped platelets. The top map in *Fig. 29* represents the image of *Fig. 28*. The fact that the lattice fringes of the Pd (we see the (*111*) lattice planes of Pd + O) are mixed with *Moiree* fringes points to the small thickness of the Pd and to the ordered nature of the underlying support phase. On the right hand side of the image,

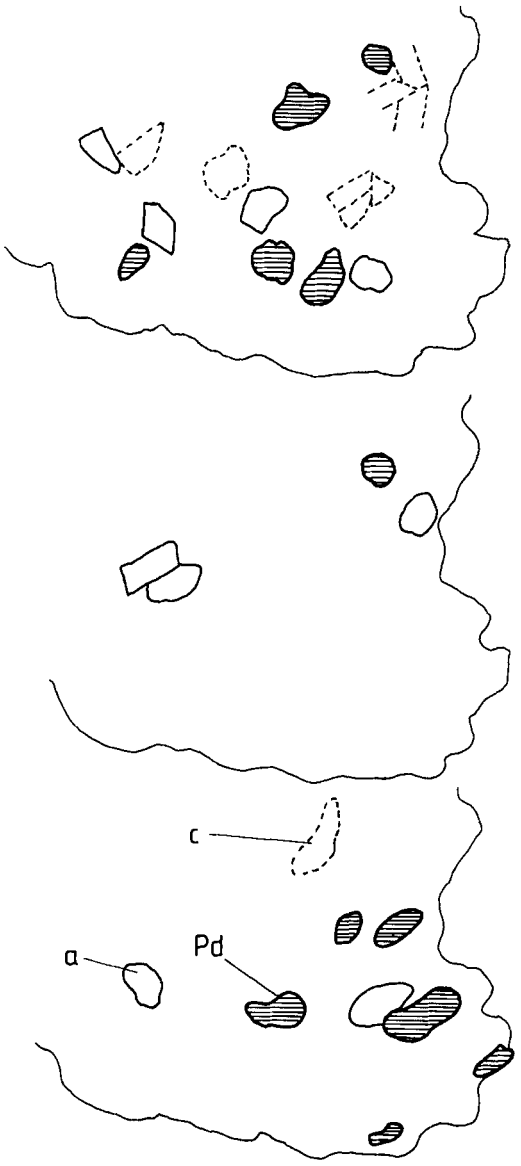

Fig. 29. *Schematic representation of the domains visible in the area imaged in* Fig. 28. To account for the sensitivity of the lattice fringes towards the correct focussing condition, which can not be fulfilled over the whole area of an uneven surface as in *Fig. 28*, the analysis of the lattice fringes was carried out with three images under slightly different focussing conditions. The top map was drawn from the image in *Fig. 28*. The patchwork-like structure of the surface composed of calcite (*c*), aragonite (*a*) and lattice-expanded Pd (Pd) can be recognized. In this extremely spatially resolved analysis of the surface of the catalyst *746*, the additional presence of $PbCO_3$ can not be excluded. It should be pointed out that these images are also typical for the Pb-free precursor (5% *E 407 R/D*) and that there is no indication for the presence of Pb within the Pd islands. The Pd seen on these images is believed to be the active and selective part of the catalyst with an intimate contact to the support.

we see two examples of intergrown calcite microcrystals. On the left hand side, we identify two areas where calcite and aragonite are intergrown. The angle between the lattice fringes is the same as between the preferential orientations seen in the diffraction pattern (*Fig. 26*, close to 60°).

Fig. 28 shows a typical situation with small domains of Ca compounds and small thin particles of the solid solution of a gas in Pd dispersed on the entire surface. Less frequently, a situation was observed as displayed in *Fig. 30*. Here, we see a large single crystal of aragonite (the (*111*) lattice planes with a distance of d = 3.42) in the center and right of the viewing area. A collection of very small crystallites of Pd compound is attached at the edge of this crystal (central part of the edge visible in *Fig. 30*). We note the perfect match of a small aragonite domain with the terminating single crystal seen in the very center of the edge. The angle between the lattice fringes corresponds to the observation in the diffraction pattern (*Fig. 26*, 30°).

The relationship between elemental Pd and aragonite can be seen from *Fig. 30*. A particle consisting of at least 5 domains of Pd in elemental form (note the difference from the Pd compound which is always a single domain on the support) is attached to a very large single crystal of aragonite. The fringes of the support arise from the aragonite (*111*) lattice planes, the Pd fringes arise from the Pd (*111*) planes. The inset shows the details of the polycrystalline microcrystal which is not detectable by XRD. The single crystal terminates in steps perpendicular to the lattice fringes. The coverage of these steps may well be the calcium carbonate hydroxide. Contamination from the microscope seems less likely, since the layer is not present over the Pd particle. The inset demonstrates a possible function of the hydroxide overlayer. It forms a kind of bed around a metal particle and increases the area of intimate contact between support and metal particle. The inset also shows that the Pd fringes are orientated towards the aragonite fringes in an angle of 35°. We see the direct contact between the metal atoms and the support $CaCO_3$.

On the single crystal, several dark areas are visible. These contrast maxima arise from very thin Pd platelets with extremely weak lattice fringes (not visible in the photographic reproduction of *Fig. 30*). These fringes allow to identify the Pd platelets as PdH or Pd + O.

The observations of the high-resolution TEM are summarised in the schematic view of the catalyst structure displayed in *Fig. 31*. The microcrystalline structure of the support is not shown, we concentrate here on the Pd compounds. Needles of clean support and of $PbCO_3$ (top in *Fig. 31*) are present as well as agglomerates of Pd (bottom in *Fig. 31*). Most frequently, needles were observed with metal particles in contact with the support. Two types of metal particles can be distinguished. One type forms flat platelets of several nm in diameter which are attached flat on the support surface (larger type in *Fig. 31*, center). Its (*111*) lattice planes are *ca.* 5% wider than in elemental Pd, and this type is believed to be the solid solution of O seen in the XPES data (crystallographically it is indistinguishable from β-PdH which is also stated in the discussion given above; for chemical reasons the presence of the hydride in the non-activated form of the catalyst is excluded). The other type of Pd consists of microdomains of elemental Pd forming three-dimensional aggregates which are attached to edges of large crystallites in the needles.

With EDA, Pb is detected besides Pd on the needles depicted in the center of *Fig. 31*. It is not possible to locate the Pb more exactly, *i.e.* it is not possible to decide which type of Pd contains Pb.

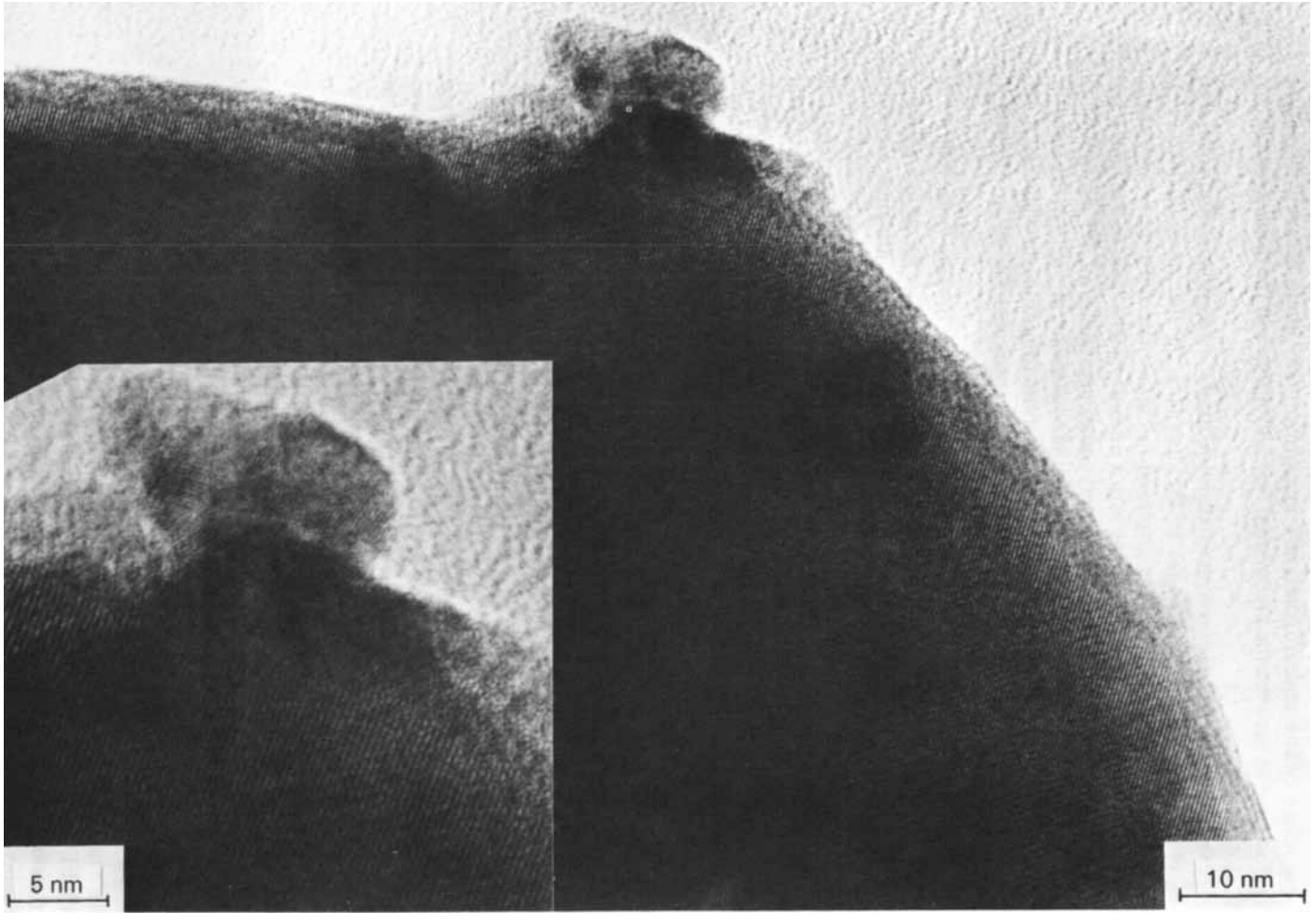

Fig. 30. *High-resolution TEM of a large single crystal of aragonite* ((*111*) plane lattice fringes) *with a small Pd particle attached to it.* The inset shows that this small particle consists of at least five domains of elemental Pd ((*111*) lattice fringes). In the inset, it can be seen how the terminating Pd-atoms are attached to the aragonite. Note in the large image how the single crystal terminates in a stepped structure to generate the smooth overall shape and to reduce the defect energy. The thin overlayer is not due to contamination in the microscope but probably represents the calcium hydroxycarbonate.

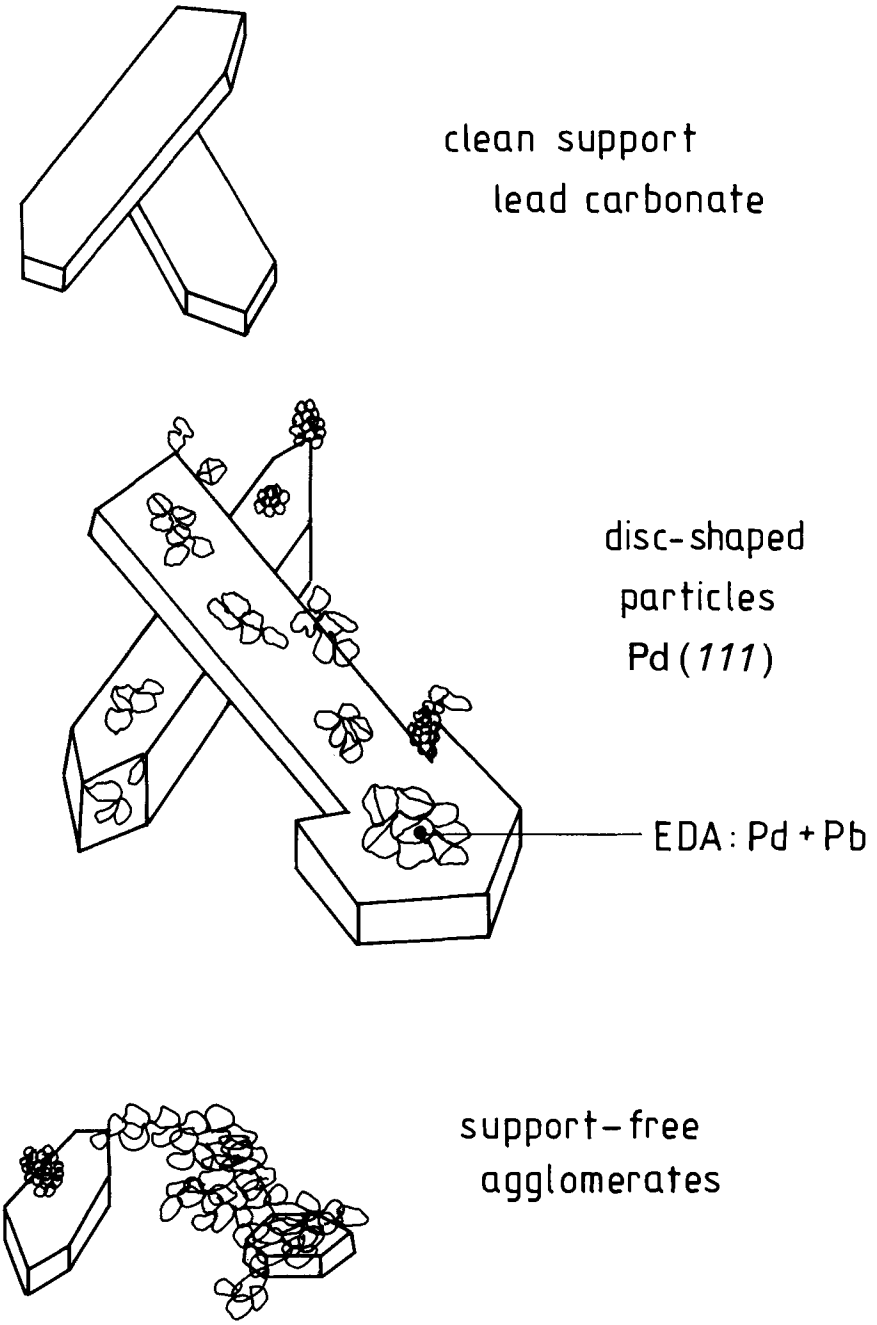

Fig. 31. *Schematic representation of the structure of the needles in the industrial catalyst* 746. Three types of needles can be distinguished. Two types of Pd (central sketch) were identified: disk-shaped single particles attached to the support and complex spherical particles with little support interactions. In addition, large agglomerates of support-free Pd are also present (bottom).

4. Discussion. – 4.1. *The Role of the Pb Additive.* The microstructure of the catalysts may be described in a crude image from the evidence discussed so far. The role of the Pb additive, however, is less clear than the structure of the Pd ingredient. In particular, the failure to observe any influence of the Pb on the structure of the Pd compound on the support by TEM and XRD makes it difficult to consider a bulk modification of the Pd by Pb. We, thus, envisage a local modification of the Pd surface by Pb. The Pb may be incorporated in surface-near regions of the Pd particles and form a solid solution Pd + O + Pb. In an other picture, the Pb may be adsorbed on certain sites of the Pd particles.

Two possible modes of action for the additive may be considered. The Pb could modify the electronic structure of the adjacent Pd-atoms such that either the activity towards H may be changed or that the adsorption properties for the substrate may be modified. The second model assumes that Pb is adsorbed specifically at certain sites of the Pd surface. These sites may be the most active locations for H transfer. By chemical reduction of the Pb-atoms, these sites may be irreversibly blocked. As a result, the total hydrogenation activity for the organic substrates may be reduced suitably to allow selective chemisorption of the substrate to govern the overall reaction on the modified and partly desactivated Pd. We would like to mention that a similar situation has recently been described in the system Ni-zeolite with Pb poisoning [26]. There, it was found that the Pb did not reduce the hydrogenation activity per site, but changed the number of sites in such a way that the selectivity for hydrogenation increased. On the other hand, the rate of hydrogenolysis was strongly influenced by the presence of Pb. These findings point to a modification of the geometric properties of a reducing surface (*e.g.* by selective site blocking) rather than an electronic modification of the hydrogenation sites. Supporting observations were made with alkali promoters on Pd supported catalysts [27]. The promoters showed little influence on the dispersion of Pd and covered only a small fraction of the Pd surface. Their influence on H_2 sorption was negligible, but CO adsorption was drastically influenced. The unselective hydrogenation of CO to CH_4 was markedly reduced by the alkali promoters.

It is difficult to verify the one or the other speculation without a detailed knowledge of the chemical bonding between the organic substrate and the catalyst. In the following, we compare the electronic structures of Pd and the Pd/Pb solid solution reference system. This comparison allows to exclude several speculations without, however, giving clear evidence for the mode of action of the Pb additive. Besides a direct comparison of the valence electronic structures of the two systems, we use chemisorption of CO and H_2 as sensitive probes for the surface chemical properties. It has been shown recently that chemisorption of CO may be successfully used to investigate details of the electronic structures of alloy systems [28]. Changes in the binding energies of the adsorbed CO as well as changes in the chemisorption behaviour (molecular *vs.* dissociative) indicate modifications of the valence electronic structure of elements like Ni or Pd upon alloying with other transition metals or non-metals.

4.1.1. *The Solid Solution.* Two samples of the nominal composition $Pd_{90}Pb_{10}$ were prepared by rapid solidification by the technique of splat cooling [29]. XRD revealed a diffraction pattern similar to that of Pd with an increase in the lattice constant compared to elemental Pd (see *Sect. 3.2*). This indicates that Pb is incorporated in Pd. Very little difference between the b.e.'s (see *Table 2*) of the elements and the solid solution could be

detected by XPES. The core-level intensities gave a surface composition (after sputtering) for both preparations of $Pd_{89}Pb_{11}$ in excellent agreement with the nominal composition. ISS analysis calibrated against foils of the elements gave $Pd_{86}Pb_{14}$ indicating only little surface segregation. The system is also rather stable against segregation at higher temperature. At 800 K the composition was found by XPES to be $Pd_{85}Pb_{15}$.

4.1.2. *The Valence-Band Spectra.* In *Fig. 32*, we show the background corrected He(I) UPE spectra of the solid solution (*b*) and the constituent elements. There was very little difference between the corresponding spectra shown in *Fig. 32* and those taken with He(II) irradiation (see *Fig. 33*) and the XPE valence-band spectra. One of the reasons is the small cross section for the Pb-states in comparison to the Pd-states (the intensity scales for the spectra in *Fig. 32* are not the same for Pd and Pb). The overall features in the

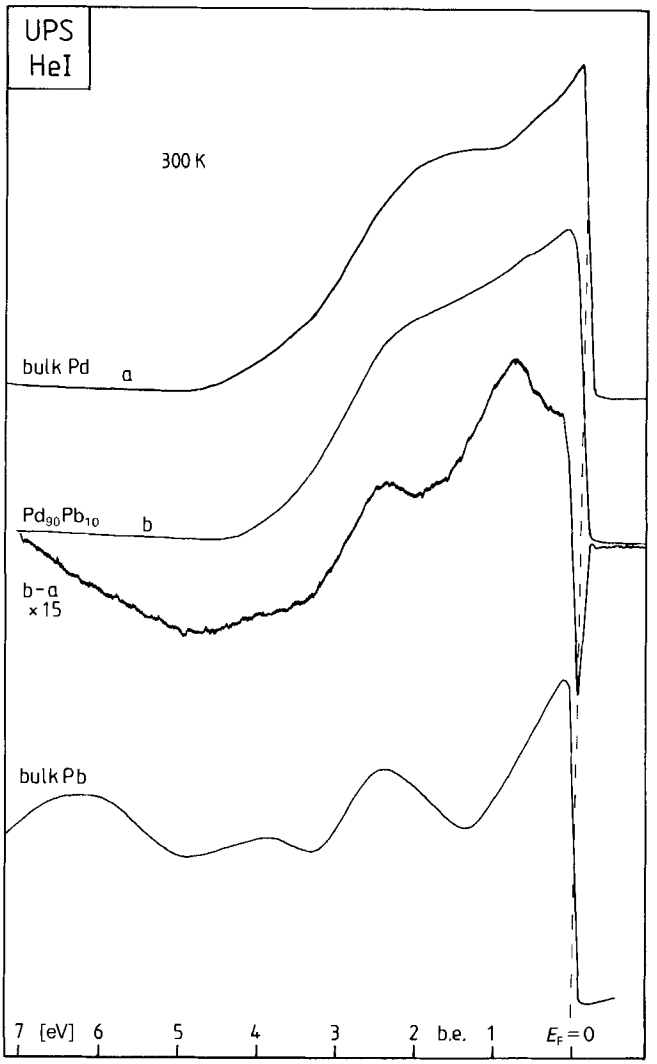

Fig. 32. *He(I) UPES data for the solid solution $Pd_{90}Pb_{10}$ and for the constituting elements.* All spectra were corrected for the background.

spectra of Pd and the solid solution are similar which is in contrast to other Pd alloys, *e.g.* with Si or Cu where shifts and changes in shape of the Pd 4d band have been observed [30]. The difference spectrum (center of *Fig. 32*) resembles the spectrum for pure Pb (bottom of *Fig. 32*). The discrepancies in the conduction band arise from the subtraction of the surface-state feature which is only present in pure Pd but not in the alloy. In addition, part of the feature between 1 and 2 eV in the difference spectrum may arise from the change of the lattice parameter of the alloy which should induce some defect states in the Pd 4d band. In summary, we observe only small differences between the spectra of the alloy and the superposition of the spectra of the constituents, *i.e.*, we see very little evidence of interaction between the two elements in the alloy.

4.1.3. *CO Adsorption.* In *Fig. 33*, the He(II) spectra of clean Pd, the alloy, and of Pb are compared with spectra of Pd and the alloy after adsorption of 8L of CO (1 Langmuir = 1-s exposure at a partial pressure of 10^{-6} Torr (= 1.33×10^{-6} mbar)) at liquid N_2

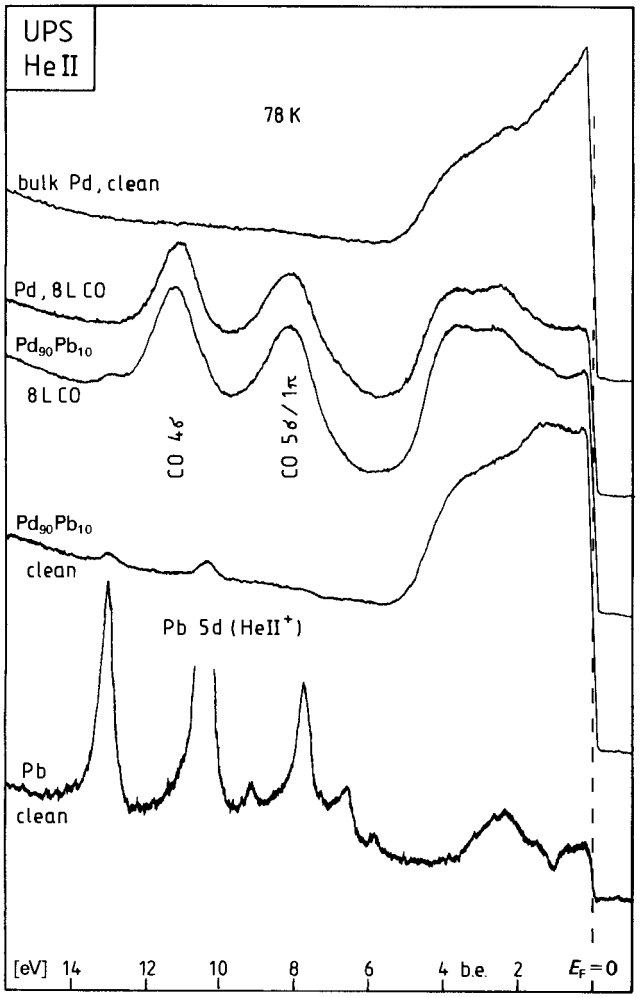

Fig. 33. *Chemisorption of CO on Pd foil and on the solid solution* $Pd_{90}Pb_{10}$. The reference spectrum for clean Pb (bottom) is dominated by satellites of the He(II) excitation of the Pb 5d core levels. Elemental Pb did not adsorb CO at 78 K.

temperature. The spectrum for pure Pb is governed by the He(II) satellite spectra of the Pb 5d-core levels. The most intense satellites are also visible in the spectrum of the alloy. We note that there is no shift for these core levels between the alloy and the element. This is in agreement with a recent study of CO adsorption on Pd-rich Cu alloys [32], but disagrees with the findings for CO adsorption for very dilute Pd/Cu alloys [31]. The small amount of Pb in our alloy does not dilute the Pd sufficiently to modify the chemisorption properties of individual Pd sites by separating them from each other (loss of the cooperative Pd-Pd interaction).

The CO spectra shown in *Fig. 33* are typical for molecular adsorption in both the Pd/Pb alloy and the pure Pd foil. This and the fact that none of the three molecular orbitals of CO is shifted clearly indicate that the adsorption properties of the alloy and of Pd metal are identical. The slightly coverage-dependent b.e.'s are reported in *Table 5*. The presence of the Pb does not greatly modify the adsorption properties as expected from the absence of any detectable d-band shift.

Table 5. *CO Adsorption on Pd and $Pd_{90}Pb_{10}$*

T [K]	Exposure [L]	4 σ [eV]	5 σ[a]) [eV]	Saturation coverage [%]
Sample Pd Foil				
80	1	11.0	8.1	–
80	80	11.1	8.2	100
300	1	10.8	7.9	–
300	80	10.8	7.9	74
Sample $Pd_{90}Pb_{10}$ Foil				
80	1	11.0	8.2	–
80	80	11.3	8.2	100
200	1	10.9	8.0	–
200	80	11.1	8.2	98
300	1	10.8	8.0	–
300	80	10.9	8.0	66

[a]) Coincides with the 1 π orbital.

The forms of the adsorption isotherms of the pure metal and the alloy, displayed in *Fig. 34*, are very similar and become identical, if the isotherm of the alloy is corrected for the absence of 10% of the Pd-atoms in the surface. The fact that this correction is not necessary at 200 K, although the surface composition as seen by ISS is unchanged, indicates a different temperature dependence of the adsorption maximum and, thus, a different heat of adsorption of CO on the two substrates. There is no loss of the specific coverage at both temperatures, as it was observed for the Pd/Cu alloys [31].

No CO is adsorbed on Pb under our experimental conditions. This was confirmed by a control experiment with a Pb foil. The temperature dependence of the coverage is slightly different for both substrates. *Table 5* lists some values which indicate that CO is somewhat easier desorbed from the alloy than from Pd.

Thus, CO adsorption gives little evidence for a significant modification of the adsorption properties as sampled by an unspecific adsorbent. The slightly different heats of adsorptions detected by the temperature dependences may represent different surface geometries rather than electronic effects.

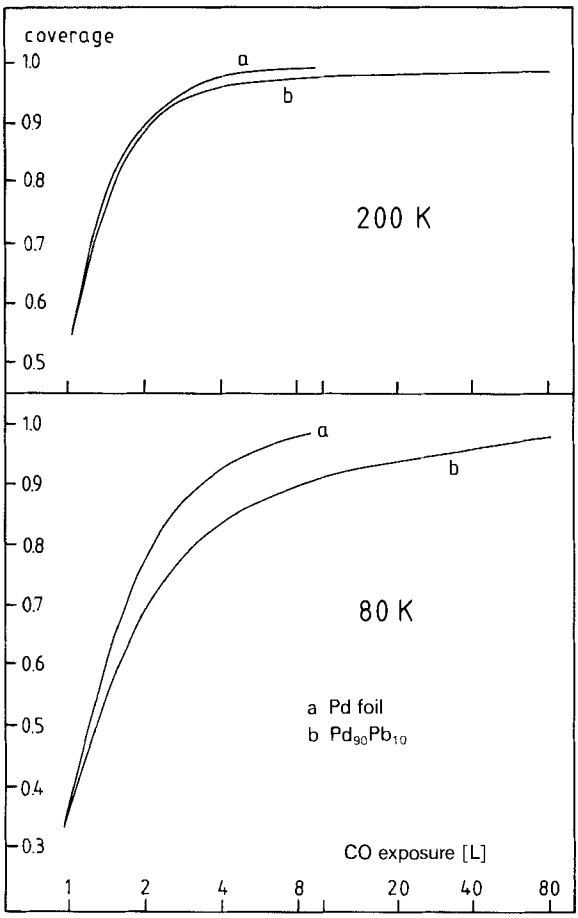

Fig. 34. *Adsorption isotherms for CO on Pd* (a) *and* $Pd_{90}Pb_{10}$ (b). The isotherms were constructed from relative coverages as determined by the area under the CO 4σ peak (see *Fig. 33*).

4.1.4. *H_2 Adsorption.* The adsorption properties of both pure Pd and the solid solution alloy for the reactant H_2 were also investigated. The results are shown in *Fig. 35*. The difference spectra of the clean substrates and the substrates after adsorption of 100 L hydrogen at 78 K are displayed. The difference spectra are again very similar and this indicates that the addition of Pb to Pd does not influence its sorption properties for H_2. The observed spectra are also very similar to a spectrum described for H_2 adsorbed on a Pd single-crystal surface [20] [33] (see indication in *Fig. 35*). The reaction of H_2 with Pd to the hydride has been described to result in a peak at lower binding energy than the one observed (see also *Fig. 35*) [20]. In both spectra, the density of states at the *Fermi* edge is reduced by the loss of the surface state and by the formation of new states between H 1s and the Pd valence band. The minima at the same energy also indicate that the valence-band structures of Pd and the Pd-Pb alloy are very similar. This is again in contrast to the observations on other Pd alloys [28] [30]. In these systems, adsorption of CO causes a

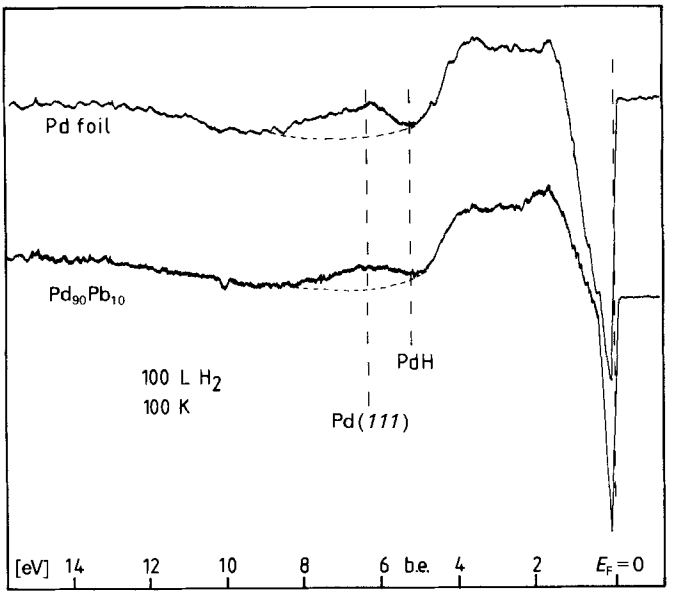

Fig. 35. *Adsorption of H_2 on Pd foil and on $Pd_{90}Pb_{10}$.* The additional states induced by chemisorption become visible in the He(II) difference spectra (adsorbed state minus clean state). The broken reference lines were taken from the literature (see text).

similar drop in the density of Pd 4d states which are, however, shifted to higher energy as a consequence of alloying (the minimum which appears in the spectra of *Fig. 35* close to the *Fermi* edge occurs in those cases at *ca.* 2 eV).

4.1.5. *Summary.* Comparison of the valence-band spectra and the adsorption properties for unspecific adsorbates CO and H_2 between Pd and the solid solution alloy $Pd_{90}Pb_{10}$ reveals that the presence of Pb does not modify the adsorption properties of the majority of sites on the alloy surface. An electronic effect of the added Pb on Pd is thus ruled out. The experiments have not probed, however, all sites on the surface of the alloy. This would require the adsorption of the organic substrates used in the catalytic testing. The Pb addition locally modifies the Pd and enhances the intrinsic selectivity of the element Pd considerably. The fact that Pb exhibits a very small electrochemical reduction potential relative to H_2 may be taken as indication that the adsorbed Pb is 'hydrogenated' on the most active sites of the Pd surface. These sites become then blocked for further hydrogenations of organic substrates.

Selectivity is discussed in the literature within the framework of two kinetic models [34]. In the first model, the triple-bond substrate is adsorbed on one site, reduced to the double-bond species, and further reduced on the same site to the single-bond final product. Selectivity occurs as a consequence of different rate constants for the two reduction steps. The selective catalyst exhibits for the first step a higher rate constant than for desorption and for the second step a lower rate constant than for desorption of the double-bond substrate. Delicate fine-tuning of the electronic properties of the catalyst sites is required in order to achieve this mode of operation. The addition of Pb to Pd metal does not modify the electronic properties of Pd and, hence, can not play the role of the

tuning agent. Any influence on the morphology as a method for tuning the sites on Pd is also excluded from XRD and EM results.

In the second model [34], the two hydrogenation steps occur on two different sites. The reduction of the triple-bond substrate takes place on a first type of sites followed in all cases by desorption of the double-bond substrate. Readsorption of this substrate on a second type of sites is followed by reduction to the final single-bond substrate. Selectivity depends in this model on the ratio of the overall rate constant (for ad-desorption and hydrogenation) for the two separate reactions. If one assumes a similar (see *Fig. 35*) and fast hydrogenation step, the selectivity depends in this model on the difference in rates of adsorption on the two types of sites. If the addition of Pb to Pd reduces the number of sites of the second type (selective for hydrogenation of the double-bond substrate), this would reduce the rate of adsorption for the second hydrogenation. Such a model would be consistent with our spectroscopic informations which give little evidence for a qualitative modification of all sites rather than show that the total number of adsorption sites is reduced. It should be pointed out that a definitive distinction between the two mechanisms suggested can only be based on kinetic data taken under steady-state conditions. The spectroscopic arguments presented here may serve, however, as a guide to the design of relevant experiments.

In the discussion presented so far, several most active sites for H transfer have been specified. In the overall reaction, three H-transfer reactions occur, one leading to reduced Pb (in the activation phase) and two to double- and single-bond organic substrates, respectively (in the reaction phase). For the selective chemisorption of Pb, it is plausible that this chemisorption in conjunction with the reduction of Pb occurs first on the most active sites (no uniform Pb film covers the surface, we assume islands of Pb located on steps and other surface heterostructures). These sites are the most active ones for hydrogenation of C=C bonds according to the two-step model of selectivity. Blocking these sites by covering them with Pb increases the selectivity towards the formation of products with double bonds. If these are also the most active sites for reduction of the triple bonds, the Pb addition may also cause a loss in activity of the reduction of the triple bonds. Pb addition forces then the reaction to proceed on still unblocked less active sites and results in a reduction of the hydrogenation rate.

4.2. *Concluding Discussion.* In the preceding sections, we have described the results of a variety of analytical techniques obtained on two types of selective catalysts, an industrial one and a model system. The differences in properties between two batches of the industrial catalyst underline the difficulty to uniquely describe the properties of 'the' catalyst. Nevertheless, we have attempted to draw a crude picture of the ingredients of the industrial catalyst. This picture focuses on the microstructure of the catalyst and considers the catalyst as a complex inorganic solid with defined bulk and surface reactivites. Which of the identified elements of the structure are the essentials for the function of the catalyst can not be decided on the grounds of our investigation. Analysis of the catalyst under operating conditions by spectroscopy and by a detailed kinetic analysis would be required.

The catalyst consists of at least seven different solid phases. These are calcite and aragonite as the bulk of the support, a covering layer of crystalline calcium carbonate-hydroxide, $PbCO_3$, at least one further Pb compound, at least one metallic Pb species and at least two Pd species with the formal oxidation state zero (Pd + O and Pd or PdH). We

omit the occasional presence of detrimental PdO. The solid solution Pd + O seems to be an important ingredient in this catalyst as well as in the widely used Pd black catalyst. The sensitivity of the quality of the catalyst towards modifications of the support can be rationalised in terms of the established structural relationship between Pd solid solution and the support. The successful support is an aggregate of domains of calcite and aragonite which are preferentially oriented such that crystal planes containing only Ca ions are parallel and form the interface layers with the noble metal particles. Such crystal planes are of suitable distance to allow the lattice-expanded Pd solid solution to be attached to the support without structural deformation. Only part of the total Pd is involved in this special relationship to the support. The rest forms aggregates of micro-crystals loosely attached to, or completely separated from, the support. This part of elemental Pd is believed not to be a desired form of the selective catalyst. It is difficult to see how this part of the noble-metal loading requires the presence of a special support for its catalytic action. Its relative abundance in the industrial catalysts can be increased by

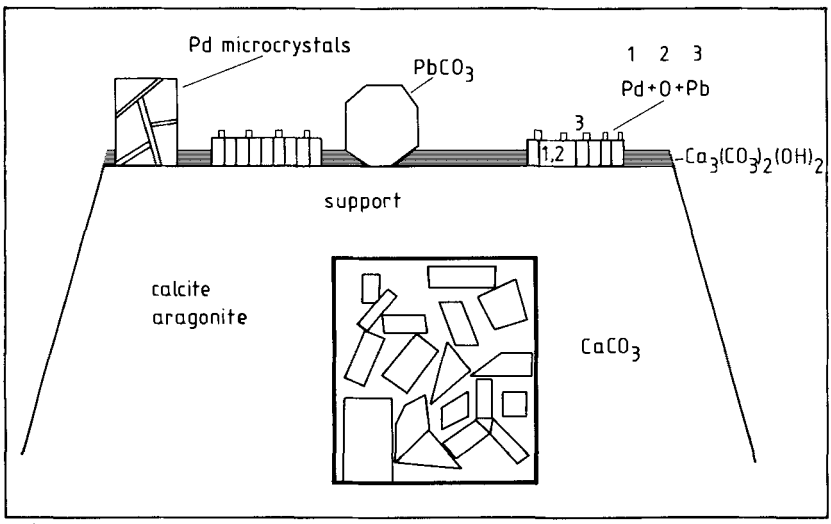

Fig. 36. *Schematic representation of the main elements identified as ingredients into an active and selective Pd hydrogenation catalyst.* The inset is a sketch of the top view on the support. It shows the microdomains of calcite and aragonite constituting the bulk of the support.

treatments such as washing with CH_2Cl_2 or thermal treatment (at *ca.* 800 K). Both treatments cause the activity to fall off drastically. The thermal treatment destroys also the solid solution Pd + O. Thermal treatment of both batches of the industrial catalysts results in the same final product of elemental Pd and zero-valent Pb indicating the similarity of the untreated precursor solids. Different qualities of the selective hydrogenation catalyst contain different amounts of the two types of Pd. The addition of Pb seems to block locally a selection of sites which is responsible for unselective (fast) hydrogenation. It was not possible to establish a quantitative relationship between the catalytic performance and either the abundance of a particular Pd species or the abundance of Pb.

These ingredients are schematically presented in *Fig. 36* which is a schematic sketch of these catalysts. The picture describes the unused catalyst. During use of this material changes are believed to occur such as the conversion from Pd + O to PdH. These reactions are seen as the reason for the failure to establish a spectroscopic criterion describing the catalytic performance in detail. The surface of the reacting catalyst is different from the surface of the unused catalyst.

The microstructure of the bulk support is indicated in the inset. It represents a top view on the grain structure of the $CaCO_3$. With *Fig. 36*, we do not want to oversimplify the nature of this catalyst. However, since the accurate measurements were only conducted on two samples we do not want to emphasize too many details which may not be typical for all of these catalysts.

We acknowledge the collaboration with *K. Steiner* from *F. Hofmann-La Roche & Co. AG*, who provided the samples of the catalysts and reference compounds. All activity tests were carried out by him, and we had many fruitful discussions with him. The collaboration of Miss *V. Geiser* and *B. Siegenthaler*, who helped with the experimental catalysts, is also gratefully acknowledged. We thank *H.-J. Güntherodt* of the Department of Physics at the University of Basel for letting us use is XRD facilities and providing the palladium lead reference samples. *R. Hauert* and *G. Indlekofer* gave us insight into some XPES/UPES results prior to publication. At *F. Hoffmann-La Roche & Co. AG*, we further thank *A. Bubendorf* for the FTIR spectra, *G. Nössberger* for the *BET* measurements, and *V. Colombo* for SEM investigations. We thank *W. Vetter* for critical discussions during the course of this work and for reading the manuscript. We are indepted to *J. M. Thomas* of University of Cambridge for letting us use his high-resolution SEM/EDX instrument.

REFERENCES

[1] H. Lindlar, *Helv. Chim. Acta* **1952,** *35*, 446.
[2] T. Fukuda, T. Kusama, *Bull. Chem. Soc. Jpn.* **1958,** *31*, 339.
[3] T. Fukuda, *Bull. Chem. Soc. Jpn.* **1958,** *31*, 343.
[4] A. B. McEven, M. J. Guttieri, W. Maier, R. M. Laine, Y. Shvo, *J. Org. Chem.* **1983,** *48*, 4436.
[5] W. Palczewska, J. Jablonski, Z. Kaszkur, *J. Mol. Catal.* **1984,** *25*, 307.
[6] J. Rajaram, A. P. S. Narula, H. P. S. Chawla, S. Dev, *Tetrahedron* **1983,** *39*, 2315.
[7] W. Palczewska, *Adv. Catal.* **1975,** *24*, 245.
[8] A. Sarkany, A. H. Weiss, L. Guczi, *J. Catal.* **1986,** *98*, 550; J. P. Boitiaux, J. Cosyns, S. Vasudevan, *Appl. Catal.* **1983,** *6*, 41.
[9] Y. Takasu, T. Akimaru, K. Kasahara, Y. Matsuda, *J. Am. Chem. Soc.* **1982,** *104*, 5249.
[10] H. Lindlar, R. Dubuis, *Org. Synth.* **1966,** *46*, 89.
[11] 'Practical Surface Analysis by Auger and X-Ray Photoelectron Spectroscopy', Eds D. Briggs and M. P. Seah, John Wiley & Sons Ltd., New York, 1983, Appendix 5.
[12] JCPDS, International Centre for Diffraction Data, 1601 Park Lane, Swarthmore. PA 19081.
[13] P. K. Gallagher, D. W. Johnson, *Thermochim. Acta* **1973,** *67*, 83.
[14] R. E. Hayes, W. J. Thomas, K. E. Hayes, *J. Catal.* **1985,** *92*, 312.
[15] L. Bonneviot, M. Che, D. Olivier, G. A. Martin, E. Freund, *J. Phys. Chem.* **1986,** *90*, 2112.
[16] J. Michalik, M. Heming, L. Kevan, *J. Phys. Chem.* **1986,** *90*, 2132.
[17] C. S. Fadley, in 'Electron Spectroscopy: Theory, Techniques and Applications', Ed. C. R. Brundle and A. B. Baker, Academic Press, London, 1978, Vol. 2, Chapt. 1.
[18] M. Peuckert, *J. Phys. Chem.* **1985,** *89*, 2481.
[19] K. S. Kim, A. F. Gossmann, N. Winograd, *Anal. Chem.* **1974,** *46*, 197.
[20] a) F. Greuter, I. Strathy, E. W. Plummer, W. Eberhardt, *Phys. Rev. B* **1986,** *33*, 736; b) D. E. Eastman, J. K. Cashion, A. C. Switendick, *Phys. Rev. Lett.* **1971,** *27*, 35.
[21] A. Fritsch, P. Légaré, *Surface Sci.* **1985,** *162*, 742; S. Kohiki, *Appl. Surface Sci.* **1986,** *25*, 81; R. Unwin, A. M. Bradshaw, *Chem. Phys. Lett.* **1978,** *58*, 58; Y. Takasu, R. Unwin, B. Tesche, A. M. Bradshaw, *Surface Sci.* **1978,** *77*, 219.

[22] Y. Takasu, T. Akimaru, Y. Matsuda, *J. Am. Chem. Soc.* **1982,** *104,* 5249.
[23] C.D. Wagner, W.M. Riggs, L.E. Davis, J.F. Moulder, G.E. Muilenberg, 'Handbook of X-Ray Photoelectron Spectroscopy', Perkin-Elmer-Corporation, Eden Prairie, Minn. 1979.
[24] K. Noack, unpublished results.
[25] R.J. Baird, C.S. Fadley, S.K. Kawamoto, M. Mehta, R. Alvarez, J.A. Silva, *Anal. Chem.* **1976,** *48,* 843.
[26] M.F. Ribeiro, F.R. Ribeiro, P. Dufresne, C. Marcilly, *J. Mol. Catal.* **1986,** *35,* 227.
[27] J.S. Rieck, A.T. Bell, *J. Catal.* **1986,** *100,* 305.
[28] R. Hauert, Dissertation, Basel 1986; R. Hauert, P. Oelhafen, R. Schlögl, H.-J. Güntherodt, *Solid State Commun.* **1985,** *55,* 583.
[29] H.-J. Güntherodt, 'Metallic Glasses', in 'Festkörperprobleme' (Advances in Solid State Physics), Ed. J. Treusch, Vieweg, Braunschweig, 1977, Vol. 17, p. 25.
[30] C.F. Hague, P. Oelhafen, J.-H. Güntherodt, in 'Amorphous Metallic Alloys', Ed. F.E. Luborski, Butterworths, London, 1983, p. 126ff.
[31] N. Martesson, R. Nyholm, H. Calén, J. Hedman, B. Johansson, *Phys. Rev. B* **1981,** *24,* 1725.
[32] J. Hedman, M. Klasson, R. Nilsson, C. Nordling, M.F. Sorokina, O.I. Kljushnikov, S.A. Nemnonov, V.A. Trapeznikov, V.G. Zyryanov, *Phys. Scr.* **1971,** *4,* 195.
[33] H. Conrad, G. Ertl, J. Küppers, E.E. Latta, *Surface Sci.* **1976,** *58,* 578.
[34] G.C. Bond, G. Webb, P.B. Wells, J.M. Winterbottom, *J. Catal.* **1962,** *1,* 74.